The Southern hemisphere midlatitude circulation response to rapid adjustments and sea surface temperature driven feedbacks

T. Wood[1], A. C. Maycock[1], P. M. Forster[1], T. B. Richardson[1], T. Andrews[2], O. Boucher[3], G. Myhre[4], B. H. Samset[4], A. Kirkevåg[5], J.-F. Lamarque[6], J. Mülmenstädt[7], D. Olivié[5], T. Takemura[8], D. Watson-Parris[9]

[1] School of Earth and Environment, University of Leeds, Leeds, United Kingdom

[2] Met Office Hadley Centre, Exeter, United Kingdom

[3] Institut Pierre-Simon Laplace, Sorbonne Université, 4 place Jussieu, Paris, France

[4] CICERO Center for International Climate and Environmental Research – Oslo, Norway

[5] Norwegian Meteorological Institute, Oslo, Norway

[6] NCAR/UCAR, Boulder, USA

[7] Universität Leipzig, Germany. Now at Pacific Northwest National Laboratory, Richland, Washington, USA

[8] Kyushu University, Fukuoka, Japan

[9] Atmospheric, Oceanic and Planetary Physics, Department of Physics, University of Oxford, Oxford, UK

Corresponding author email: pm11tw@leeds.ac.uk

Abstract:

Rapid adjustments – the response of meteorology to external forcing while sea surface temperatures (SST) and sea ice are held fixed – can affect the midlatitude circulation and contribute to long-term forced circulation responses in climate simulations. This study examines rapid adjustments in the Southern hemisphere (SH) circulation using nine models from the Precipitation Driver and Response Model Intercomparison Project (PDRMIP), which perform fixed SST and coupled ocean experiments for five perturbations: a doubling of carbon dioxide (2xCO2), a tripling of methane (3xCH4), a five-fold increase in sulphate aerosol (5xSO4), a ten-fold increase in black carbon aerosol (10xBC) and a 2% increase in solar constant (2%Sol). In the coupled experiments, the SH eddy-driven jet shifts poleward and strengthens for forcings that produce global warming (and vice versa for 5xSO4), with the strongest response found in austral summer. In austral winter, the responses project more strongly onto a change in jet strength. For 10xBC, which induces strong shortwave absorption, the multi-model mean (MMM) rapid adjustment in DJF jet latitude is ~75% of the change in the coupled simulations. For the other forcings, which induce larger SST changes, the effect of SST-mediated feedbacks on the SH circulation is larger than the rapid adjustment. Nevertheless, for these perturbations the magnitude of the MMM jet shift due to the rapid adjustment is still around 25-33% of that in the coupled experiments. The results demonstrate the need to understand the mechanisms for rapid adjustments in the midlatitude circulation, in addition to the effect of changing SSTs.

1. Introduction

The midlatitude atmospheric circulation is expected to alter under climate change (Shaw et al., 2016 and references therein). Such changes could have significant implications for the characteristics of extratropical cyclones (Tamarin-Brodsky and Kaspi, 2017) and regional changes in extremes, such as droughts, heat waves, and wind storms (Field et al., 2012; Li et al., 2018; Steptoe et al., 2018). However, there remain large uncertainties in the quantitative understanding of the midlatitude circulation response to changes in greenhouse gases (GHGs), aerosols and natural climate forcings (Collins et al. 2013; Santer et al., 2013; Staten et al., 2012) and associated climate feedbacks such as through clouds and water vapour (Ceppi and Shepherd, 2017; Voigt and Shaw, 2015, 2016; Voigt et al., 2019). In the Southern hemisphere (SH), reanalysis datasets and climate models show a strengthening and poleward shift of the midlatitude eddy-driven jet (EDJ) over recent decades (e.g. Polvani et al., 2011; Barnes and Polvani, 2013), and a shift towards a more positive Southern Annular Mode (SAM) index (Marshall, 2003) with associated changes in storm tracks (e.g. Yin, 2005; Chen and Held, 2007; Bender et al., 2012), Rossby wave breaking (Ndarana et al., 2012), and atmospheric blocking (Dennison et al., 2016). The historical trends in SH circulation have been attributed to the effects of ozone depletion (primarily affecting the austral summer season) and rising greenhouse gases (GHG) (Karpechko and Maycock et al., 2018 and references therein), with a potentially important role for internal climate variability (Garfinkel et al., 2015). Over the 21st century, general circulation models (GCMs) project further shifts in the SH midlatitude circulation associated with the effects of ozone recovery and scenario-dependent changes in GHGs (e.g Ceppi and Hartmann, 2013; Barnes and Polvani, 2013; Barnes et al., 2014; Kushner et al., 2001; Previdi and Liepert, 2007). While these major drivers

69 are broadly known, the quantification of the importance of different forcings on the SH
70 circulation remains uncertain. For example, there has been debate in the literature
71 around the importance of anthropogenic aerosols for SH circulation trends (Gillett et
72 al., 2013; Steptoe et al., 2016; Rotstayn, 2013; Rotstayn et al., 2014; Choi et al., 2019).

73 The response of the eddy-driven jets (EDJ) to forcing is dependent on the
74 spatial pattern of surface and atmospheric temperature changes (Butler et al., 2010;
75 Ceppi and Shepherd, 2017; Harvey et al., 2014, 2015; Murphy et al., 2002). Although
76 the sign of the projected SH EDJ shift is generally robust across different climate
77 models, they simulate a range of magnitudes of response to the same forcing scenario
78 (Barnes and Polvani, 2013; Barnes et al., 2014; Grise and Polvani, 2014a). Grise and
79 Polvani (2014a, 2016) showed that intermodel differences in the SH circulation
80 response to an abrupt quadrupling in CO_2 (4xCO2) can only be partly explained by
81 differences in global surface air temperature (GSAT) responses and instead might be
82 explained, to varying degrees depending on region and season, by increases in
83 midlatitude and subtropical static stabilities (see also Butler et al., 2010), and changes
84 to surface and upper-tropospheric/lower-stratospheric equator-to-pole temperature
85 gradients. Harvey et al. (2014) found that in CMIP5 models a significant fraction of the
86 model spread in projected SH storm track changes over the 21st century was linearly
87 congruent with spread in upper- and lower-level temperature gradient responses. The
88 radiative effects of clouds are also important for SH midlatitude circulation trends
89 (Ceppi et al., 2014; Grise and Polvani, 2014b; Albern et al., 2019). The EDJ response
90 to forcing is likely to be seasonally varying due to the seasonal cycle in the background
91 circulation (McGraw and Barnes, 2016) and seasonally-dependent factors such
92 stratospheric polar vortex trends (Ceppi and Shepherd, 2019). Given these various
93 results, modelled changes in the midlatitude circulation therefore cannot be expected

to simply scale with GSAT (Grise and Polvani, 2014a, 2016, 2017; Ceppi et al., 2018), rendering efforts to constrain measures such as equilibrium climate sensitivity of limited value for projections of midlatitude circulation.

One emerging topic is the relative importance of so-called “direct or rapid adjustment” and “indirect or slow feedback” processes for the midlatitude circulation response to forcing. Rapid atmospheric adjustments - which occur when a forcing is introduced but sea surface temperatures (SST) and sea ice are held fixed - are well known to affect the top of atmosphere energy budget through changes to clouds, thermal structure and surface fluxes (Sherwood et al., 2015; Smith et al., 2018); however, the influence on large-scale circulation is underexplored. Grise and Polvani (2014c) decomposed the atmospheric circulation response to 4xCO2 in CMIP5 models into a rapid adjustment and an SST-driven component. While the rapid adjustment contributed a poleward shift of the EDJ, the overall response to 4xCO2 was dominated by SSTs, which are also responsible for the asymmetric midlatitude circulation response between hemispheres. Grise and Polvani (2017) further decomposed the SH circulation response to 4xCO2 by season and found that the midlatitude circulation shifts poleward on a similar timescale to GSAT change in austral summer (DJF), but adjusts more quickly than GSAT in austral winter (JJA). Ceppi et al. (2018) showed that nearly all of the SH EDJ response to 4xCO2 occurs within the first decade, despite less than 50% of the eventual quasi-equilibrium GSAT change occurring within this time. They also used a single GCM run in coupled and fixed-SST modes to separate rapid adjustments and the SST-mediated response. However, most of these studies have primarily focused on the response to increasing CO_2, so the relative importance of rapid adjustments and SST-driven feedbacks for the responses to other forcing agents are less well known. A recent study has shown

that rapid adjustments to aerosol forcing contribute to changes in the location of the Hadley cell edge in the SH (Zhao et al., 2020), suggesting there may also be a role for the midlatitude circulation.

Idealised forcing studies allow a detailed examination of the circulation response to a single climate driver and an assessment of the differences in response across GCMs. However, a significant limitation is that most of the existing literature relies on the 4xCO2 experiment from CMIP5 and does not explore the responses to other major forcings such as non-CO_2 GHGs, aerosols and natural forcings. This study seeks to fill this gap by examining rapid adjustments and slow feedbacks in the SH midlatitude circulation in response to a number of idealised climate perturbations using output from the Precipitation Driver and Response Model Intercomparison Project (PDRMIP, Myhre et al., 2017).

2. Data and Methods

2.1 Models and Simulations

We use output from nine models participating in the Precipitation Driver and Response Model Intercomparison Project (PDRMIP) (Table S1; Myhre et al., 2017). Each model performed a control run using present day conditions or pre-industrial conditions (see Table S1), and five idealised abrupt single forcing experiments: 1) a doubling of carbon dioxide concentrations (2xCO2), 2) a tripling of methane concentrations (3xCH4), 3) a five-fold increase in sulphate aerosol concentrations or emissions (5xSO4), 4) a ten-fold increase in black carbon aerosol concentrations or emissions (10xBC) and 5) a two percent increase in the solar constant (2%Sol). The distribution of the aerosol concentration or emissions perturbations is shown in Figure

142 2 of Myhre et al. (2017). The scaling factors for the five idealised perturbations were
143 chosen so that each experiment induced a similar magnitude of effective radiative
144 forcing (ERF) to better enable climate responses to be compared across forcing
145 agents (Smith et al, 2018). The perturbations are not necessarily designed to be based
146 on a realistic future atmospheric concentration scenario. In practice, the magnitudes
147 of the multi-model mean (MMM) ERFs for 2xCO2, 5xSO4 and 2%Sol are comparable
148 to within ~10%, whereas the ERFs for 3xCH4 and 10xBC are around three times
149 smaller.

150 All experiments are performed in two model configurations: one set has sea-
151 surface temperatures and sea ice fixed to the control climatology (fSST) enabling the
152 rapid adjustments to be diagnosed; the second set includes a coupled ocean and thus
153 the full atmosphere-ocean response is captured. Note that the fSST experiments do
154 not fix land temperatures, which may be important for some regional climate
155 responses (Shaw and Voigt, 2016). The ECHAM-HAM and CESM1-CAM4 models use
156 a slab ocean and are excluded from the MMM and intermodel regression calculations.
157 The fSST experiments are integrated for at least 15 years and the coupled
158 experiments for at least 100 years (see Table S1). Responses are calculated by
159 subtracting the time mean climatology of the control simulation from the perturbed
160 experiments. The fSST responses are diagnosed as the time mean excluding the first
161 year, ensuring only the quasi-equilibrated adjusted state is captured (Richardson et
162 al., 2016). In all cases the coupled response is diagnosed using the mean of years 50-
163 100. This captures the quasi-equilibrated climate after the perturbations are applied,
164 but neglects further climate responses, for example in the deep ocean, that will evolve
165 for many hundreds of years before reaching a true equilibrium state (Caldeira and
166 Myhrvold, 2013).

The SPRINTARS and HadGEM2-ES models defined variables on pressure levels that are below the surface as missing data. Therefore, at some grid points over topography the MMM calculation excludes those models. The robustness of the MMM responses is indicated using stippling where one or more of the models disagree on the sign of change.

2.2 Midlatitude circulation response metrics

The response of the midlatitude circulation and its relation to the large-scale climate is diagnosed using metrics based on zonal winds and surface and air temperatures. The variables available from the different models to compute these diagnostics are listed in Table S2.

a. Latitude of EDJ

The maximum speed and location of the EDJ (U_{max} and ϕ_{EDJ}) is diagnosed as the speed and location of maximum zonal mean zonal wind ($\overline{U}$) at 850 hPa between 15°S and 70°S after cubically interpolating to a 0.01° latitude grid.

b. Upper- and lower-tropospheric temperature gradients

Following Harvey et al. (2014), diagnostics for upper (250 hPa) and lower (850 hPa) tropospheric temperature gradients (ΔT) are computed using the difference between the area-average temperature anomaly (T) in the tropics (30°S - 30°N) and SH polar region (60°S - 90°S):

$$\Delta T250 = T250_{(30°S\text{-}30°N)} - T250_{(60°S\text{-}90°S)} \quad (1)$$

$$\Delta T850 = T850_{(30°S\text{-}30°N)} - T850_{(60°S\text{-}90°S)} \ . \quad (2)$$

Previous studies using PDRMIP models that have focused on thermodynamic properties have often normalised metrics by GSAT or ERF to compare across the different perturbations (Richardson et al., 2019). However, since forced changes to the SH midlatitude circulation have been shown not to scale with GSAT change (e.g. Grise and Polvani, 2017; Ceppi et al., 2018) we have chosen not to normalise the circulation changes in this study.

2.3. Statistical significance

Two main methods are used to assess the robustness of the model responses; both methods have been used to evaluate multi-model ensembles in the IPCC AR5 (2013). The first method evaluates the agreement in the sign of the simulated anomalies across models. Hatching is applied where one or more models disagrees on the sign of the anomaly. The second method quantifies the magnitude of the simulated anomalies compared to internal variability. To calculate each model's internal variability in the coupled experiments, we calculate the standard deviation of consecutive 50-year means sampled from the control runs and multiply this by the square root of 2 to reflect the uncertainty due to internal variability in the difference of two 50-year means. Simulated changes are significant at the 95% level when the modulus is greater than 1.96σ, where σ is either taken from a given model or, in the case of the MMM, is the median standard deviation of the models.

For the fSST runs, a bootstrap was performed by selecting N years from the coupled control run, where N is the length of the fSST experiment in each model (see Table S1). The coupled control runs were used as they are longer than the fSST runs enabling a more comprehensive assessment of internal variability to be attained. This was repeated 10^3 times to construct a probability density function. The standard

deviation was then calculated and multiplied by the square root of 2 as before. Years are selected randomly as the fSST runs do not include any SST-mediated low frequency variability. Lastly, inter-model regressions between variables are calculated using linear least squares regression.

3. Results

3.1 Surface temperature changes

Figures 1(a-e) show the MMM zonal mean SH near-surface temperature anomalies in the coupled experiments. All the forcings induce an increase in near-surface temperature except 5xSO4, which induces cooling as expected. The MMM global and annual mean surface air temperature (GSAT) changes in the 2xCO2, 3xCH4, 5xSO4, 10xBC and 2%Sol experiments are: 2.39 K, 0.70 K, -1.82 K, 0.85 K, and 2.38 K, respectively (see Table 1). The variation in magnitude of the MMM GSAT responses is primarily a consequence of differences in effective radiative forcing (ERF) between the perturbations (Richardson et al., 2019). The MMM ERFs for 2xCO2, 3xCH4, 5xSO4, 10xBC and 2%Sol are 3.7 W m^{-2}, 1.1 W m^{-2}, -1.8 W m^{-2}, 1.3 W m^{-2} and 4.1 W m^{-2}, respectively (Tang et al., 2019). The GSAT changes also vary across models for the same experiment owing to differences in both ERF and modelled equilibrium climate sensitivity (Richardson et al., 2019). The zonal mean surface temperature anomalies show a heterogeneous pattern over the Southern hemisphere, with a small amplification in the Antarctic and larger changes at latitudes with more land mass (Dong et al., 2009; Joshi et al., 2008). However, the changes in near-surface temperature gradient across the SH in the coupled experiments are consistently smaller than in the Northern hemisphere where Arctic amplification leads

to a weakened equator-to-pole temperature gradient in the lower troposphere (not shown).

Figures 1 (f-j) show the MMM zonal mean SH near-surface temperature anomalies in the fSST simulations. The anomalies are substantially smaller than in the coupled runs at all latitudes (<20%) but, as expected, the proportionately largest responses occur over land (e.g. Antarctica) where the surface temperatures are not fixed in the models. Over Antarctica, the aerosol perturbations cause small surface temperature changes of the opposite sign to those in the coupled experiments. At latitudes that are almost exclusively covered by ocean in the SH (~40-60°S) the proportion of the temperature response that occurs in the fSST runs is very small (<10%), as expected. The GSAT anomalies in the fSST experiments are: 0.28 K, 0.07 K, -0.09 K, 0.11 K and 0.15 K (Table 1), which is around 5-10% of the corresponding changes in the coupled experiments.

3.2 Zonal mean air temperature changes

Figure 2 shows the MMM annual and zonal mean air temperature anomalies in the five perturbation experiments. Panels (a-e) show the coupled experiments, panels (f-j) show the fSST experiments and panels (k-o) show the SST-mediated response (coupled minus fSST). As seen in Figure 1, the amplitude of the tropospheric temperature anomalies vary across the perturbations. The tropospheric response is strongest for 2xCO2 and 2%Sol and weakest for 3xCH4. The magnitude of the tropospheric temperature response to 5xSO4 lies between 2xCO2 and 3xCH4, but is opposite in sign. These differences can be understood from the ERF associated with each perturbation (see Section 3.1). Nevertheless, despite the different magnitudes, all the forcings except 10xBC induce a similar pattern of tropospheric temperature

259 change in the coupled experiments, with larger anomalies in the tropical upper
260 troposphere and near the Antarctic surface. This broad pattern of tropospheric
261 temperature response is a robust feature in GCMs that accompanies changes in global
262 mean surface temperature and associated climate feedbacks (IPCC, 2013; Ceppi and
263 Shepherd, 2017).

264 The tropospheric temperature changes in 10xBC show a markedly different
265 pattern to the other perturbations (Figure 2d). Black carbon affects climate through
266 absorption of shortwave radiation and so directly heats the atmosphere while inducing
267 smaller surface temperature change (Stjern et al., 2017). The black carbon burden in
268 the experiments is spatially dependent, with emissions in the SH primarily originating
269 from biomass burning in central Africa, the Amazon and Indonesia (Myhre et al., 2017).

270 Polar lower stratospheric temperature changes have been shown to be
271 important for the tropospheric midlatitude circulation (e.g. Harvey et al., 2014;
272 Thompson and Solomon, 2002; Grise and Polvani, 2017). In the polar lower
273 stratosphere, all perturbations except 10xBC induce temperature changes in the
274 coupled experiment that are opposite in sign to the tropospheric response. The 2xCO2
275 experiment induces stronger radiative cooling in the stratosphere that increases with
276 height (Fels et al., 1980). The 10xBC perturbation induces a weak warming in the
277 Antarctic lower stratosphere.

278 The fSST temperature anomalies due to the five perturbations show markedly
279 different patterns from the coupled experiments (Figures 2 (f-j)). The enhanced tropical
280 upper tropospheric temperature changes found for 2xCO2, 3xCH4, 5xSO4 and 2%Sol
281 are largely absent in the fSST experiments, indicating this structure is predominantly
282 due to SST-driven feedbacks through moist convective adjustment in the tropics

(Figures 2 (k-o)). Instead the tropospheric temperature changes in the 2xCO2, 3xCH4, 5xSO4 and 2%Sol fSST experiments are weaker and more homogeneous. 2xCO2 is the only perturbation that induces strong radiative cooling in the stratosphere in the fSST experiments (Smith et al., 2018). There is also a stratospheric heating response in 2%Sol, which is mainly due to shortwave absorption by ozone. In contrast to 2xCO2, 3xCH4, 5xSO4 and 2%Sol, the fSST temperature response in 10xBC more closely resembles the coupled experiment showing that the direct shortwave absorption by black carbon dominates the anomalous atmospheric heating. The difference between the coupled and fSST temperature anomalies for 10xBC reveals a pattern that resembles the response to the other forcings (Figures 2 (k-o)), with a magnitude similar to the coupled 3xCH4 experiment. This is consistent with the similar magnitudes of ERF and GSAT change for the 10xBC and 3xCH4 perturbations (Table 1). The overall temperature response in the coupled 10xBC experiment is therefore relatively less affected by SST-driven feedbacks and is predominantly due to shortwave absorption.

The results in Figures 1 and 2 demonstrate the uneven distribution of surface and atmospheric temperature changes induced by the different climate drivers, as well as the important role of SSTs in determining these changes particularly for 2xCO2, 3xCH4, 5xSO4 and 2%Sol. The coincident responses of the midlatitude circulation are investigated in the following sections.

3.3 Zonal wind changes

3.3.1 Austral summer (DJF)

The MMM $\overline{U}$ anomalies in austral summer (DJF) are shown in Figure 3. Panels (a-e) show the coupled experiments, panels (f-j) show the fSST experiments and

panels (k-o) show the SST-mediated response (coupled minus fSST). In austral summer, the $\overline{U}$ climatology (grey contours) comprises a single well-defined eddy-driven jet (EDJ) near 50°S (Nakamura and Shimpo, 2004). In the coupled experiments, all five perturbations induce a dipole of tropospheric $\overline{U}$ anomalies between 60°S and 30°S, which indicates a shift in the latitude of the EDJ (see Section 3.4). The largest tropospheric $\overline{U}$ changes occur in 2xCO2 and 2%Sol and the weakest changes occur in 3xCH4. The forcings that induce tropospheric warming show a poleward shift and strengthening of the EDJ in DJF, and vice versa for 5xSO4. In the stratosphere, there is a region of westerly anomalies (easterlies for 5xSO4) across the extratropics which peaks around 50-60°S and a secondary maximum anomaly of the same sign near the subtropical jet around 30°S, 100-200 hPa.

All the fSST perturbation experiments (Figure 3 (f-j)) except 3xCH4 also show a dipole pattern of tropospheric $\overline{U}$ anomalies in southern midlatitudes. For each experiment, the dipole change is of the same sign as in the coupled experiments (i.e. a poleward shift for 2xCO2, 10xBC and 2%Sol and an equatorward shift for 5xSO4). In the 3xCH4 experiment a rapid adjustment in zonal winds is not detectable. The stratospheric zonal wind changes at high latitudes in DJF are not robust across the models in the 10xBC experiment, and are of the same sign but muted in the 2xCO2, 5xSO4 and 2%Sol experiments compared to the equivalent coupled runs.

Figure 4 shows longitude-latitude SH zonal wind anomalies at 850 hPa (U_{850}) in the five perturbation experiments. The left and right columns in Figure 4 show the coupled and fSST experiments, respectively. For all perturbations there is a high degree of longitudinal symmetry in the midlatitude zonal wind responses in the coupled experiments. This is consistent with there being a single well-defined EDJ in austral

summer associated with a circumpolar storm track (Nakamura and Shimpo, 2004). There is less consistency across the models in the coupled response to 10xBC particularly between 60°-180°E, which could be partially explained by the differences in black carbon burden in the different models (Stjern et al., 2017). The models agree on the sign of the U_{850} anomalies in the region of the EDJ in the other coupled forcing experiments.

The fSST experiments (Figures 4 (f-j)) also show a high degree of longitudinal symmetry in the midlatitude U_{850} changes. Although the responses are smaller, and the agreement across the models lower than in the coupled experiments, the MMM pattern of U_{850} anomalies in the fSST experiments strongly resemble the coupled responses particularly in midlatitudes. The rapid adjustment is proportionately largest for 10xBC, where in the southern Indian ocean sector and south of Australia the fSST U_{850} anomalies are comparable in magnitude to the fully coupled response and up to around 60% of the magnitude near South America. For 2xCO2, 5xSO4 and 2%Sol the magnitude of the U_{850} anomalies in the fSST experiments is typically around 30-60% of that in the coupled experiments in the important EDJ region where the response is most robust.

The individual model wind anomalies can be seen in Figure 5, which shows zonal mean U_{850} ($\overline{U_{850}}$) anomalies relative to the climatological EDJ latitude in each model. The IPSL-CM5A model shows the strongest $\overline{U_{850}}$ responses in the coupled experiments for 2xCO2, 3xCH4, 5xSO4 and 2%Sol. The CCCma model shows the strongest response in 10xBC and also shows the second strongest response in all other experiments except for 3xCH4. The fSST experiments generally show similar but weaker $\overline{U_{850}}$ responses (Figures 5(f-j)). There are some exceptions where

individual models show an opposite response compared to the coupled experiments; this includes SPRINTARS for the 10xBC experiment and CCCma for the 3xCH4 experiment.

In summary, this section has shown the rapid adjustments of the SH midlatitude circulation in DJF resemble a weaker version of the coupled responses.

3.3.2 Austral winter (JJA)

Figure 6 shows the MMM $\overline{U}$ responses to the five perturbations in JJA in the same layout as Figure 3. In austral winter, the climatology (grey contours) shows a strong subtropical jet that is merged with the EDJ (Nakamura and Shimpo, 2004). In contrast to the deep, equivalent barotropic dipole zonal wind anomalies found in DJF, the JJA responses in the coupled experiments show a deep monopole structure in the troposphere, which maximises on the southern flank of the westerly wind maximum. This projects more strongly onto a change in jet strength than in DJF (see Section 3.4). The EDJ responses to 3xCH4 and 5xSO4 are weaker, though small poleward and equatorward shifts, respectively, are found. The zonal wind response to 10xBC is comparatively small in the lower troposphere in JJA, with the largest $\overline{U}$ response found in the upper troposphere and stratosphere. The stratospheric zonal wind responses are of the same sign to those in DJF, but maximise at lower latitudes in JJA near the subtropical jet.

A weaker midlatitude zonal wind response to forcing in JJA, as compared to DJF, has been previously identified in response to increased CO_2 (e.g. Grise and Polvani, 2016), stratospheric water vapour changes (Maycock et al., 2013) and in idealised models with applied thermal forcings (McGraw and Barnes, 2016). Despite

377 the smaller magnitude, there is high agreement across the models on the sign of the
378 zonal wind changes in the region of the EDJ.

379 The fSST experiments show $\overline{U}$ responses in JJA that resemble the deep
380 monopole wind anomaly found in the coupled experiments for the 2xCO2, 3xCH4 and
381 5xSO4 perturbations (Figures 6 (f-j)). In contrast, the tropospheric changes in the
382 2%Sol experiment show only a strengthening of westerlies near the subtropical jet, but
383 no robust response in the midlatitudes. The fSST response to 10xBC is also less
384 robust in JJA. This suggests that changes to SSTs are important for the SH midlatitude
385 $\overline{U}$ responses to 2%Sol and 10xBC in JJA.

386 Figure 7 shows the U_{850} anomalies in JJA. The U_{850} responses are generally
387 less longitudinally symmetric than in DJF (cf. Figure 4), with the westerly anomalies
388 (easterlies for 5xSO4) being more equatorward in the Indian and Pacific Ocean
389 sectors and more poleward in the Atlantic sector. The fSST responses in JJA (Figures
390 7 (f-j)) show the 2xCO2 and 3xCH4 perturbations induce the strongest U_{850} response
391 in the southern Indian Ocean and South Pacific sectors and a comparatively weaker
392 response in the South Atlantic. The rapid adjustment to 10xBC is proportionately
393 stronger than for the other forcings in both JJA and DJF. Interestingly, to the south of
394 Australia in the 10xBC fSST experiment the response is opposite in sign to the coupled
395 anomalies. This indicates that the SST-mediated changes must override the direct
396 atmospheric response in these regions. As seen in Figure 6j, in contrast to the other
397 perturbations the U_{850} anomalies in the 2%Sol fSST experiment are weak and not
398 consistent in sign across the models.

399 Figure 8 shows the latitudinal profiles of $\overline{U_{850}}$ in JJA for the different models.
400 There is a consistent sign of $\overline{U_{850}}$ anomalies across the models in the coupled

experiments and, except for IPSL-CM5A, all the models show smaller zonal wind changes than in DJF. IPSL-CM5A appears to respond differently, showing a relatively strong poleward jet shift in all the experiments that produce global mean warming. The response to 5xSO4 in IPSL-CM5A is more consistent with the other models. The different response in IPSL-CM5A may be related to the exceptional warming in the southern Indian Ocean produced by the model found to be associated with unrealistic cloud-ocean feedbacks (Rowell, 2019; Rowell and Chadwick, 2018). The climatological jet position is also the farthest equatorward in IPSL-CM5A compared to the other models. A statistical relationship across models between the climatological jet latitude and forced poleward shifts in the jet has been found in austral winter (Simpson and Polvani, 2016); however, further analysis of the links to climatological jet position is beyond the scope of this paper.

The U_{850} responses in the fSST experiments are less consistent across the models, with some responding with the opposite sign such as IPSL-CM5A in the 3xCH4 experiment and SPRINTARS in the 5xSO4 and 2%Sol experiments. On average, the fSST U_{850} anomalies in JJA are smaller in magnitude and less consistent in sign across the models than in DJF.

3.4 Jet latitude and speed

This section puts the SH zonal wind changes shown in section 3.3 into the context of changes in the latitude and speed of the EDJ. Figure 9 shows the EDJ latitude and speed anomalies in DJF for the five perturbation experiments for the individual models and the MMM. Note that SPRINTARS produces a broad jet without a well-defined maximum and hence there is a large error on the estimate of the EDJ latitude so it is excluded from the MMM calculation.

Figure 9 shows a consistent poleward shift and strengthening of the EDJ across the models in the DJF season for the 2xCO2 and 2%Sol experiments, and the consistent equatorward shift and weakening of the EDJ in the 5xSO4 experiment. In the MMM, the EDJ shifts poleward by ~2° and strengthens by ~0.7 m s^{-1} in the coupled 2xCO2 and 2%Sol experiments. There is an equal and opposite MMM response of the jet speed in 5xSO4, but a smaller equatorward jet shift of ~1.5°. The MMM changes in 10xBC show a poleward shift and increase in jet speed which is around half the magnitude of 2xCO2 and 2%Sol (1.4° and 0.3 m s^{-1}). In all the coupled experiments, the sign of jet shift in DJF is consistent across the models and the MMM response is significant compared to internal variability. The same is true for jet speed except for the 3xCH4 experiment, which produces a nonsignificant MMM change, and for 10xBC where two models simulate a reduction in jet speed.

As in previous sections, the rapid adjustment in DJF is proportionately largest for 10xBC, with a magnitude of ~75% and ~90% for the MMM jet shift and jet speed changes, respectively, compared to the coupled experiment. In the other experiments, the magnitude of the rapid adjustment is a smaller yet substantial fraction of the overall coupled responses (typically 20-30% of the jet shift and 20-35% of jet speed). Furthermore, across all models and all experiments there is a significant correlation between the jet shift (φ_{max}) in the fSST and coupled experiments with a pooled $R^2(\varphi_{fSST(ALL)}, \varphi_{coupled(ALL)})_{DJF}$ = 0.30 (P = .003). For the jet speed (U_{max}) anomalies the pooled $R^2(U_{fSST(ALL)}, U_{coupled(ALL)})_{DJF}$ = 0.37 (P < .001). This suggests that part of the intermodel spread in the DJF jet shift and jet speed responses to the perturbations can be interpreted as being due to spread in the rapid adjustment.

Figure 10 shows the EDJ latitude and speed anomalies for JJA. There is a less consistent picture of the responses to the perturbations than was found in DJF. Nevertheless, consistent with the results in section 3.3, the MMM responses in JJA tend to project more strongly onto a change in EDJ strength, with larger anomalies than in DJF, whilst there are smaller changes in EDJ latitude compared to DJF by around a factor of two. Interestingly, the coupled jet shift to 5xSO4 is opposite in sign and significant in JJA and the change in jet speed is smaller than in DJF, in contrast to the other experiments. The rapid adjustment accounts for a larger proportion of the overall coupled changes in JJA than in DJF in the 2xCO2 experiment. In contrast to DJF, there is a weak and nonsignificant relationship between the jet shift and jet speed anomalies in the fSST and coupled experiments in JJA. This suggests that in JJA the intermodel spread in responses in the coupled simulations is predominantly driven by other factors than rapid adjustments.

3.5 Relationship to temperature gradients

In the extratropics, the meridional temperature gradient is proportional to the vertical wind shear through thermal wind balance. Harvey et al. (2014) found that in CMIP5 models differences in upper- and lower-level temperature gradients could explain a significant fraction of the intermodel spread in projected SH storm track changes over the 21st century. Here we examine the changes to temperature gradients in the PDRMIP experiments to determine the differences in the rapid adjustment and coupled zonal wind responses discussed above.

Figure 11 shows the annual mean upper- (250hPa) and lower- (850hPa) tropospheric meridional temperature gradient anomalies (ΔT) for the five climate perturbations in the coupled and fSST experiments. A negative (positive) anomaly

shows a reduction (increase) in the tropics-to-pole temperature gradient. There were found to be only small seasonal differences (see Supplemental Figures S1 and S2), partly because polar amplification is smaller in the SH than in the Arctic, so for simplicity the changes in annual mean temperature gradients are shown.

The models agree on the sign of ΔT_{250} in all the coupled experiments. The few models that show a negative ΔT_{850} for some perturbations are those which produce larger polar amplification (CESM1-CAM4, CESM1-CAM5). CESM1-CAM4 is a consistent outlier, which may be related to it using a simplified slab ocean model. As was done for the anomalies in jet latitude and jet speed, the slab ocean models have been excluded from the MMM. All the coupled experiments show a greater increase in ΔT_{250} than in ΔT_{850}, predominantly due to the large tropical upper tropospheric temperature changes ($r(\Delta T_{250}, T_{250,trop} > 0.87$ for all experiments, see Table S3). Similar differences between ΔT_{850} and ΔT_{250} in the SH were shown by Harvey et al. (2014) using CMIP5 models.

For all the experiments except 10xBC, the rapid adjustment in ΔT_{850} and ΔT_{250} is comparatively small, which is a consequence of the direct tropospheric heating induced by the forcings being weak and fairly uniform across the SH (Figure 2). SST feedbacks therefore dominate the overall changes in ΔT_{850} and ΔT_{250} for those perturbations. While there are larger temperature changes in the troposphere and lower stratosphere in the 10xBC fSST experiment (Figure 2), in the tropics these changes peak in the lower stratosphere above 250 hPa and it is only in the subtropics that larger temperature anomalies penetrate into the upper troposphere. Hence, the MMM rapid adjustment in ΔT_{250} is near-zero for 10xBC. There are two outliers, however, with CCCma showing a strong negative ΔT_{250} and HadGEM2 showing a

positive ΔT_{250}. These models have the largest black carbon burden of all the PDRMIP models (Stjern et al., 2017) and are both driven by aerosol emissions rather than concentrations. This suggests there are differences in the distribution of black carbon and hence tropospheric heating between the two models. An inspection of the individual model zonal mean air temperature responses reveals that CCCma produces strong upper-tropospheric and stratospheric warming in a pattern that resembles the MMM (not shown). However, the zonal mean response to 10xBC in HadGEM2 more closely resembles the response to 2xCO2, producing cooling in the stratosphere. This cooling may be caused by increased stratospheric water vapour in the HadGEM2 model. Except for 10xBC, the intermodel spread in both ΔT_{250} and ΔT_{850} is consistently larger in the coupled experiments than for fSST, reflecting the increase in model spread due to differences in climate feedbacks. For most of the perturbations, the different responses of SSTs are therefore the dominant cause of the intermodel spread in ΔT_{250} and ΔT_{850}.

In the coupled experiments, ΔT_{250} and ΔT_{850} are significantly correlated across all models and experiments in both DJF and JJA ($r(\Delta T_{250}, \Delta T_{850})_{DJF} = 0.87$ ($P < .001$); $r(\Delta T_{250}, \Delta T_{850})_{JJA} = 0.75$ ($P < .001$)). This is higher than the correlation between ΔT_{250} and ΔT_{850} in the SH across CMIP5 models (0.45 and 0.50 for DJF and JJA, respectively; Harvey et al., 2014). The correlation between ΔT_{250} and ΔT_{850} means that a regression of zonal wind responses onto either index yields qualitatively similar results. We proceed by examining the relationship between the zonal wind responses and ΔT_{850} across the models, with the caveat that in these experiments using this method we cannot distinguish the relative importance of changes to upper and lower level temperature gradients.

Figure 12 shows the fraction of inter-model variance in ΔU_{850} that is explained by ΔT_{850}, defined as the coefficient of determination (R^2). The fraction of variance explained is up to 80-90% in the EDJ region in all of the coupled experiments except 3xCH4. When a regression is performed across all coupled models and all perturbation experiments (Figure 12f), a significant relationship is found across the entire midlatitude region, with around 50-90% of the variance in local midlatitude ΔU_{850} responses explained by ΔT_{850}. This indicates that the regression onto ΔT_{850} is a useful measure for capturing much of the model spread in midlatitude circulation responses (cf. Harvey et al., 2014).

In general the perturbations that generate the largest changes in temperature gradients (2xCO2 and 2%Sol) also show the largest zonal wind responses (Figures 2 and 3), as expected from thermal wind balance. To determine if there are different intermodel relationships between ΔU_{850} and ΔT_{850} for the perturbations, Figure 13 shows the regression of ΔU_{850} against ΔT_{850} for the five perturbations. As the strongest and most consistent responses of the EDJ to the forcings occur in austral summer, we focus on DJF.

The spatial pattern of the intermodel regression between ΔU_{850} and ΔT_{850} in the coupled experiments is similar across all forcings despite the different magnitudes of responses and spatial patterns shown earlier. The patterns resemble those shown in Figure 4 with an enhanced low level temperature gradient (positive ΔT_{850}) being associated with a dipole ΔU_{850} pattern with stronger westerlies on the poleward flank of the jet and weaker westerlies on the equatorward flank. While the magnitudes of this pattern are largely similar across the five perturbations, there is a suggestion of a weaker regression coefficient in the 5xSO4 experiment, which could be due to the

544 hemispheric asymmetry of the forcing (Richardson et al. 2019). There may also be a
545 difference in the sensitivity of the zonal wind response to tropospheric cooling, as in
546 5xSO4, as compared to the warming produced by the other forcings.

547 The intermodel regression applied to the fSST experiments reveals a similar
548 dipole pattern of midlatitude ΔU_{850} response (Figure 13(g-k)); however, the magnitude
549 of the regression slope is around double that found in the coupled experiments. This
550 means that the ΔU_{850} responses in the fSST experiments are proportionately larger
551 than would be predicted by ΔT_{850} using the relationship derived from the coupled
552 experiments. While the rapid adjustment accounts for a minor part of the total coupled
553 response for most of the perturbations (except 10xBC), it is proportionately larger than
554 expected from the associated differences in ΔT_{850}. This is interesting and suggests
555 that the processes captured within the rapid adjustment, such as changes to clouds,
556 affect the midlatitude circulation in a manner not captured by a simple measure of
557 large-scale temperature gradient change. Broadly similar differences between the
558 coupled and fSST regressions is seen in JJA (see Supplemental Figure S3). A
559 regression of SH zonal mean air temperature onto ΔT_{850} in the coupled simulations
560 reveals a tropospheric pattern that is dominated by warming in the tropics and
561 midlatitudes (Figure S4(a-e)). However, in the fSST simulations, the pattern of
562 temperature anomalies regressed onto ΔT_{850} is markedly different, with a
563 warming/cooling dipole in the lower troposphere in mid/high latitudes (Figure S4(f-j)).
564 This hints towards a possible reason for the different relationships of ΔU_{850} to ΔT_{850} in
565 the fSST and coupled experiments.

566

4. Conclusions

This study has analysed the rapid adjustment (i.e. the meteorological response to forcing in the absence of SST and sea ice changes) and coupled atmosphere-ocean response of the Southern hemisphere (SH) midlatitude circulation to five idealised climate perturbations: 2xCO2, 3xCH4, 5x sulphate aerosol, 10x black carbon aerosol and +2% solar constant. Previous studies have predominantly focused on rapid adjustments to increased CO_2 (e.g. Grise and Polvani 2014a, 2014b, 2016, 2017; Ceppi and Shepherd 2017), so the novelty of this study lies in its consideration of a broader set of climate perturbations applied in nine global climate models. The rapid adjustment occurs as a result of atmospheric and land surface heating, including changes to latent heating and surface fluxes, while the coupled response is mediated by SST changes.

In the coupled experiments, the response of the SH circulation projects more strongly onto a shift in the EDJ in austral summer, while in winter the response projects more strongly onto changes in jet strength. This is similar to other studies examining the seasonality of the SH midlatitude circulation response to a constant year-round forcing (e.g. Maycock et al., 2013; McGraw and Barnes, 2016). These seasonal differences could be explained by differences in the barotropic responses between seasons, with a stronger upper-level barotropic response in summer, including changes to horizontal wave propagation and breaking (Nie et al., 2016). Barotropic Rossby wave breaking transports eddy momentum and so affects the position and speed of the EDJ (Robinson, 2006). In DJF, the SH EDJ is more zonally symmetric, narrower and stronger than in JJA, when the climatological westerlies extend further toward the subtropics especially in the Pacific sector (Ceppi and Hartmann, 2013;

Nakamura and Shimpo, 2004). Our results corroborate this, with more regional heterogeneity in the low-level zonal wind responses in JJA than in DJF. The results highlight the need to consider the seasonality of the midlatitude circulation response to forcing.

In DJF, the magnitude of the EDJ shift due to the rapid adjustment is ~20-30% of the coupled response for most of the perturbations except 10xBC where the rapid adjustment is 75% of the coupled jet shift. Hence, SST feedbacks exert an important control on the midlatitude circulation response to forcings that induce substantial global surface temperature changes. While the rapid adjustment in jet latitude in DJF is statistically significant in some models, the magnitude of the multi-model mean is small compared to internal variability for all perturbations than BCx10, so it is very unlikely that rapid adjustments in the SH midlatitude circulation could be observed. Nevertheless, for all experiments there is strong consistency in the sign of the jet latitude and speed anomalies across models, which is unlikely to be a result of internal variability. The proportionately stronger rapid adjustment to 10xBC indicates that the response is less coupled to surface temperature changes and is strongly influenced by absorption of shortwave radiation by black carbon. The magnitude of the rapid adjustment to 2xCO2 is similar to previous studies (e.g. Grise and Polvani 2014c) and also shows the rapid adjustment is comparable for methane, sulphate (though opposite in sign) and solar forcing, despite them acting through different radiative mechanisms (e.g. the extent of stratospheric cooling/heating). Despite the aerosol forcing being concentrated in the Northern hemisphere (Richardson et al., 2019), the perturbations still induce detectable changes in the SH circulation in both the rapid adjustment and coupled experiments. Integrated assessment models simulate substantial changes in emissions of aerosols such as black carbon and sulphate over

616 the coming decades. These results suggest this could impact the large-scale
617 circulation in the Southern hemisphere, though there remains debate around the role
618 of aerosol forcing for historical observed SH climate (Gillett et al., 2013; Steptoe et al.,
619 2018; Choi et al., 2019).

620 A variance analysis shows that up to 80-90% of the intermodel spread in local
621 midlatitude 850 hPa zonal wind responses (ΔU_{850}) in DJF is linearly congruent with
622 the spread in the 850 hPa tropics-to-pole temperature gradient anomaly (ΔT_{850}), with
623 comparable spatial patterns for all five perturbations. However, the gradient of the
624 relationship between ΔU_{850} and ΔT_{850} is around a factor of two larger for the rapid
625 adjustment than the equivalent coupled experiment, so the magnitude of the rapid
626 adjustment in circulation is proportionately larger than would be predicted from the
627 ΔU_{850} - ΔT_{850} relationship in the coupled experiments. This is interesting and suggests
628 that the processes captured within the rapid adjustment, such as land temperature
629 changes and clouds, are affecting the midlatitude circulation in a manner that cannot
630 be quantitatively captured by a simple measure of large-scale temperature gradient
631 change. This also demonstrates why common global climate change measures, such
632 as GSAT, are generally not useful measures for determining regional midlatitude
633 climate change (Grise and Polvani, 2016; Ceppi et al., 2018). The results demonstrate
634 the need to understand both rapid adjustments and SST-mediated feedbacks to fully
635 understand the SH midlatitude circulation response to forcing.

636

Data Availability Statement

The PDRMIP model output is publicly available (for data access, visit http://www.cicero.uio.no/en/PDRMIP/PDRMIP-data-access).

Acknowledgements

TW was funded by a PGR studentship from the NERC SPHERES Doctoral Training Partnership (NE/L002574/1). ACM was funded by a NERC Independent Research Fellowship (NE/M018199/1). ACM and PMF were funded by the European Union's Horizon 2020 Research and Innovation Programme under grant agreement 820829 (CONSTRAIN) and UKRI NERC grant NE/N006038/1 (SMURPHS). T. T. was supported by the supercomputer system of the National Institute for Environmental Studies, Japan, and JSPS KAKENHI Grant Number JP19H05669. D. O. and A. K. were supported by the Norwegian Research Council through the projects EVA (229771), EarthClim (207711/E10), NOTUR (nn2345k), and NorStore (ns2345k). T. A. was supported by the Joint UK BEIS/Defra Met Office Hadley Centre Climate Programme (GA01101). B. H. S. and G. M. were funded by the Research Council of Norway, through the grant NAPEX (229778). O. B. acknowledges HPC resources from TGCC under the gencmip6 allocation provided by GENCI (Grand Equipement National de Calcul Intensif). The authors thank Paulo Ceppi and one anonymous reviewer for their constructive comments that improved the article.

References

Albern, N., Voigt, A. and Pinto, J.G. 2019. Cloud-Radiative Impact on the Regional Responses of the Midlatitude Jet Streams and Storm Tracks to Global Warming. *Journal of Advances in Modeling Earth Systems*. [Online]. **11**(7),pp.1940–1958.

Barnes, E.A., Barnes, N.W., Polvani, L.M., Barnes, E.A., Barnes, N.W. and Polvani, L.M. 2014. Delayed Southern Hemisphere Climate Change Induced by Stratospheric Ozone Recovery, as Projected by the CMIP5 Models. *Journal of Climate*. [Online]. **27**(2),pp.852–867.

Barnes, E.A. and Polvani, L. 2013. Response of the midlatitude jets, and of their variability, to increased greenhouse gases in the CMIP5 models. *Journal of Climate*. [Online]. **26**(18),pp.7117–7135.

Bender, F.A.M., Ramanathan, V. and Tselioudis, G. 2012. Changes in extratropical storm track cloudiness 1983-2008: Observational support for a poleward shift. *Climate Dynamics*. [Online]. **38**(9–10),pp.2037–2053.

Butler, A.H., Thompson, D.W.J. and Heikes, R. 2010. The steady-state atmospheric circulation response to climate change-like thermal forcings in a simple general circulation model. *Journal of Climate*. [Online]. **23**(13),pp.3474–3496.

Caldeira, K. and Myhrvold, N.P. 2013. Projections of the pace of warming following an abrupt increase in atmospheric carbon dioxide concentration. *Environmental Research Letters*. [Online]. **8**(3),p.034039.

Ceppi, P. and Hartmann, D.L. 2013. On the speed of the eddy-driven jet and the width of the hadley cell in the southern hemisphere. *Journal of Climate*. [Online].

26(10),pp.3450–3465.

Ceppi, P. and Shepherd, T.G. 2017. Contributions of climate feedbacks to changes in atmospheric circulation. *Journal of Climate*. [Online]. **30**(22),pp.9097–9118.

Ceppi, P. and Shepherd, T.G. 2019. The Role of the Stratospheric Polar Vortex for the Austral Jet Response to Greenhouse Gas Forcing. *Geophysical Research Letters*. [Online]. **46**(12),pp.6972–6979.

Ceppi, P., Zappa, G., Shepherd, T.G. and Gregory, J.M. 2018. Fast and slow components of the extratropical atmospheric circulation response to CO2 forcing. *Journal of Climate*. [Online]. **31**(3),pp.1091–1105.

Ceppi, P., Zelinka, M.D. and Hartmann, D.L. 2014. The response of the Southern Hemispheric eddy-driven jet to future changes in shortwave radiation in CMIP5. *Geophysical Research Letters*. [Online]. **41**(9),pp.3244–3250.

Chen, G. and Held, I.M. 2007. Phase speed spectra and the recent poleward shift of Southern Hemisphere surface westerlies. *Geophysical Research Letters*. [Online]. **34**(21),p.L21805.

Choi, J., Son, S.W. and Park, R.J. 2019. Aerosol versus greenhouse gas impacts on Southern Hemisphere general circulation changes. *Climate Dynamics*. [Online]. **52**(7–8),pp.4127–4142.

Collins, M., Knutti, R., Arblaster, J., Dufresne, J.-L., Fichefet, T., Friedlingstein, P., Gao, X., Gutowski, W.J., Johns, T., Krinner, G., Shongwe, M., Tebaldi, C., Weaver, A. and Wehner, M. 2013. Long-term Climate Change: Projections, Commitments and Irreversibility *In*: T. F. Stocker, D. Qin, G.-K. Plattner, M.

Tignor, S. K. Allen, J. Boschung, A. Nauels, Y. Xia, V. Bex and P. M. Midgley, eds. *Climate Change 2013 - The Physical Science Basis. Contribution of Working Group I to the Fifth Assessment Report of the Intergovernmental Panel on Climate Change* [Online]. Cambridge: Cambridge University Press, pp. 1029–1136

Dennison, F.W., McDonald, A. and Morgenstern, O. 2016. The influence of ozone forcing on blocking in the Southern Hemisphere. *Journal of Geophysical Research*. [Online]. **121**(24),pp.14358–14371.

Dong, B., Gregory, J.M. and Sutton, R.T. 2009. Undestanding land-sea warming contrast in response to increasing greenhouse gases. Part I: Transient adjustment. *Journal of Climate*. [Online]. **22**(11),pp.3079–3097.

Fels, S.B., Mahlman, J.D., Schwarzkopf, M.D. and Sinclair, R.W. 1980. Stratospheric sensitivity to perturbations in ozone and carbon dioxide: radiative and dynamical response. *Journal of the Atmospheric Sciences*. **37**(10),pp.2265–2297.

Field, C.B., Barros, V., Stocker, T.F., Dahe, Q., Jon Dokken, D., Ebi, K.L., Mastrandrea, M.D., Mach, K.J., Plattner, G.K., Allen, S.K., Tignor, M. and Midgley, P.M. 2012. *Managing the risks of extreme events and disasters to advance climate change adaptation: Special report of the intergovernmental panel on climate change*.

Garfinkel, C.I., Waugh, D.W. and Polvani, L.M. 2015. Recent Hadley cell expansion: The role of internal atmospheric variability in reconciling modeled and observed trends. *Geophysical Research Letters*. **42**(24),pp.10824–10831.

Gillett, N.P., Fyfe, J.C. and Parker, D.E. 2013. Attribution of observed sea level

724 pressure trends to greenhouse gas, aerosol, and ozone changes. *Geophys.*
725 *Res. Lett*. [Online]. **40**,pp.2302–2306.

726 Grise, K.M. and Polvani, L.M. 2016. Is climate sensitivity related to dynamical
727 sensitivity? *Journal of Geophysical Research*. [Online]. **121**(10),pp.5159–5176.

728 Grise, K.M. and Polvani, L.M. 2014a. Is climate sensitivity related to dynamical
729 sensitivity? A Southern Hemisphere perspective. *Geophysical Research Letters*.
730 [Online]. **41**(2),pp.534–540.

731 Grise, K.M. and Polvani, L.M. 2014b. Southern hemisphere cloud-dynamics biases
732 in CMIP5 models and their implications for climate projections. *Journal of*
733 *Climate*. [Online]. **27**(15),pp.6074–6092.

734 Grise, K.M. and Polvani, L.M. 2014c. The response of midlatitude jets to increased
735 CO<inf>2</inf>: Distinguishing the roles of sea surface temperature and direct
736 radiative forcing. *Geophysical Research Letters*. [Online]. **41**(19),pp.6863–6871.

737 Grise, K.M. and Polvani, L.M. 2017. Understanding the time scales of the
738 tropospheric circulation response to abrupt CO2forcing in the Southern
739 Hemisphere: Seasonality and the role of the stratosphere. *Journal of Climate*.
740 [Online]. **30**(21),pp.8497–8515.

741 Harvey, B.J., Shaffrey, L.C. and Woollings, T.J. 2015. Deconstructing the climate
742 change response of the Northern Hemisphere wintertime storm tracks. *Climate*
743 *Dynamics*. [Online]. **45**(9–10),pp.2847–2860.

744 Harvey, B.J., Shaffrey, L.C. and Woollings, T.J. 2014. Equator-to-pole temperature
745 differences and the extra-tropical storm track responses of the CMIP5 climate

models. *Climate Dynamics*. [Online]. **43**(5–6),pp.1171–1182.

Joshi, M.M., Gregory, J.M., Webb, M.J., Sexton, D.M.H. and Johns, T.C. 2008. Mechanisms for the land/sea warming contrast exhibited by simulations of climate change. *Climate Dynamics*. [Online]. **30**(5),pp.455–465.

Karpechko, A.Y., Maycock, A.C., Abalos, M., Akiyoshi, H., Arblaster, J.M., Garfinkel, C.I., Rosenhof, K.H. and Sigmond, M. 2018. Stratospheric Ozone Changes and Climate, Chapter 5 in Scientific Assesment of Ozone Depletion: 2018 *In*: *Global Ozone Research and Monitoring Project–Report No. 58* [Online].

Kushner, P.J., Held, I.M. and Delworth, T.L. 2001. Southern Hemisphere Atmospheric Circulation Response to Global Warming. *Journal of Climate*. [Online]. **14**,pp.2238–2249.

Li, C., Michel, C., Seland Graff, L., Bethke, I., Zappa, G., Bracegirdle, T.J., Fischer, E., Harvey, B.J., Iversen, T., King, M.P., Krishnan, H., Lierhammer, L., Mitchell, D., Scinocca, J., Shiogama, H., Stone, D.A. and Wettstein, J.J. 2018. Midlatitude atmospheric circulation responses under 1.5 and 2.0g°C warming and implications for regional impacts. *Earth System Dynamics*. [Online]. **9**(2),pp.359–382.

Marshall, G.J. 2003. Trends in the Southern Annular Mode from observations and reanalyses. *Journal of Climate*. [Online]. **16**(24),pp.4134–4143.

Maycock, A.C., Joshi, M.M., Shine, K.P. and Scaife, A.A. 2013. The circulation response to idealized changes in stratospheric water vapor. *Journal of Climate*. **26**(2),pp.545–561.

McGraw, M.C. and Barnes, E.A. 2016. Seasonal sensitivity of the eddy-driven jet to tropospheric heating in an idealized AGCM. *Journal of Climate*. [Online]. **29**(14),pp.5223–5240.

Murphy, B.F., Pettré, P. and Simmonds, I. 2002. *Effects of changing baroclinicity on the southern hemisphere extratropical circulation* [Online].

Myhre, G., Forster, P.M., Samsmset, B.H., Odnebrog, Sillmann, J., Aalbergsjø, S.G., Andrews, T., Boucher, O., Faluvegi, G., Fläschner, D., Iversen, T., Kasoar, M., Kharin, V., Kirkevag, A., Lamarque, J.F., Olivié, D., Richardson, T.B., Shindell, D., Shine, K.P., Stjern, C.W., Takemura, T., Voulgarakis, A. and Zwiers, F. 2017. PDRMIP: A precipitation driver and response model intercomparison project-protocol and preliminary results. *Bulletin of the American Meteorological Society*. [Online]. **98**(6),pp.1185–1198.

Nakamura, H. and Shimpo, A. 2004. *Seasonal variations in the Southern Hemisphere storm tracks and jet streams as revealed in a reanalysis dataset*.

Ndarana, T., Waugh, D.W., Polvani, L.M., Correa, G.J.P. and Gerber, E.P. 2012. Antarctic ozone depletion and trends in tropopause Rossby wave breaking. *Atmospheric Science Letters*. [Online]. **13**(3),pp.164–168.

Nie, Y., Zhang, Y., Chen, G. and Yang, X.-Q. 2016. Delineating the Barotropic and Baroclinic Mechanisms in the Midlatitude Eddy-Driven Jet Response to Lower-Tropospheric Thermal Forcing. *Journal of the Atmospheric Sciences*. [Online]. **73**(1),pp.429–448.

Polvani, L.M., Waugh, D.W., Correa, G.J.P. and Son, S.W. 2011. Stratospheric ozone depletion: The main driver of twentieth-century atmospheric circulation

changes in the Southern Hemisphere. *Journal of Climate*. [Online]. **24**(3),pp.795–812.

Previdi, M. and Liepert, B.G. 2007. Annular modes and Hadley cell expansion under global warming. *Geophysical Research Letters*. [Online]. **34**(22),p.L22701.

Richardson, T.B., Forster, P.M., Maycock, A.C., Smith, C.J., Wood, T., Andrews, T., Boucher, O., Faluvegi, G., Fläschner, D., Hodnebrog, Ø., Kasoar, M., Kirkevåg, A., Lamarque, J.-F., Mülmenstädt, J., Myhre, G., Olivié, D., Samset, B.H., Shawki, D., Shindell, D., Takemura, T. and Voulgarakis, A. 2019. Efficacy of climate forcings in PDRMIP models. *Journal of Geophysical Research: Atmospheres*. [Online],p.Submitted.

Richardson, T.B., Samset, B.H., Andrews, T., Myhre, G. and Forster, P.M. 2016. An assessment of precipitation adjustment and feedback computation methods. *Journal of Geophysical Research*. [Online]. **121**(19),pp.11608–11619.

Robinson, W.A. 2006. On the Self-Maintenance of Midlatitude Jets. *Journal of the Atmospheric Sciences*. [Online]. **63**(8),pp.2109–2122.

Rotstayn, L.D. 2013. Projected effects of declining anthropogenic aerosols on the southern annular mode. *Environmental Research Letters*. [Online]. **8**(4),p.044028.

Rotstayn, L.D., Plymin, E.L., Collier, M.A., Boucher, O., Dufresne, J.L., Luo, J.J., Von Salzen, K., Jeffrey, S.J., Foujols, M.A., Ming, Y. and Horowitz, L.W. 2014. Declining aerosols in CMIP5 projections: Effects on atmospheric temperature structure and midlatitude jets. *Journal of Climate*. [Online]. **27**(18),pp.6960–6977.

814 Rowell, D.P. 2019. An Observational Constraint on CMIP5 Projections of the East
815 African Long Rains and Southern Indian Ocean Warming. *Geophysical*
816 *Research Letters*. [Online]. **46**(11),pp.6050–6058.

817 Rowell, D.P. and Chadwick, R. 2018. Causes of the uncertainty in projections of
818 tropical terrestrial rainfall change: East Africa. *Journal of Climate*. [Online].
819 **31**(15),pp.5977–5995.

820 Santer, B.D., Painter, J.F., Bonfils, C., Mears, C.A., Solomon, S., Wigley, T.M.L.,
821 Gleckler, P.J., Schmidt, G.A., Doutriaux, C., Gillett, N.P., Taylor, K.E., Thorne,
822 P.W. and Wentz, F.J. 2013. Human and natural influences on the changing
823 thermal structure of the atmosphere. *Proceedings of the National Academy of*
824 *Sciences*. [Online]. **110**(43),pp.17235–17240.

825 Shaw, T.A., Baldwin, M., Barnes, E.A., Caballero, R., Garfinkel, C.I., Hwang, Y.-T.,
826 Li, C., O'Gorman, P.A., Rivière, G., Simpson, I.R. and Voigt, A. 2016. Storm
827 track processes and the opposing influences of climate change. *Nature*
828 *Geoscience*. [Online]. **9**(9),pp.656–664.

829 Shaw, T.A. and Voigt, A. 2016. Understanding the links between subtropical and
830 extratropical circulation responses to climate change using aquaplanet model
831 simulations. *Journal of Climate*. [Online]. **29**(18),pp.6637–6657.

832 Sherwood, S.C., Bony, S., Boucher, O., Bretherton, C., Forster, P.M., Gregory, J.M.
833 and Stevens, B. 2015. Adjustments in the forcing-feedback framework for
834 understanding climate change. *Bulletin of the American Meteorological Society*.
835 **96**(2),pp.217–228.

836 Simpson, I.R. and Polvani, L.M. 2016. Revisiting the relationship between jet

837 position, forced response, and annular mode variability in the southern
838 midlatitudes. *Geophysical Research Letters*. [Online]. **43**(6),pp.2896–2903.

839 Smith, C.J., Kirkevåg, A., Andrews, T., Samset, B.H., Lamarque, J.-F., Hodnebrog,
840 Ø., Mülmenstädt, J., Stier, P., Soden, B.J., Smith, C.J., Takemura, T., Shindell,
841 D., Kramer, R.J., Watson-Parris, D., Richardson, T., Faluvegi, G., Kharin, V.,
842 Forster, P.M., Olivié, D., Kasoar, M., Fläschner, D., Myhre, G., Voulgarakis, A.
843 and Boucher, O. 2018. Understanding Rapid Adjustments to Diverse Forcing
844 Agents. *Geophysical Research Letters*. [Online]. **45**(21),pp.12,023-12,031.

845 Staten, P.W., Rutz, J.J., Reichler, T. and Lu, J. 2012. Breaking down the
846 tropospheric circulation response by forcing. *Climate Dynamics*. [Online]. **39**(9–
847 10),pp.2361–2375.

848 Steptoe, H., Jones, S.E.O. and Fox, H. 2018. Correlations Between Extreme
849 Atmospheric Hazards and Global Teleconnections: Implications for Multihazard
850 Resilience. *Reviews of Geophysics*. [Online]. **56**(1),pp.50–78.

851 Steptoe, H., Wilcox, L.J. and Highwood, E.J. 2016. Is there a robust effect of
852 anthropogenic aerosols on the southern annular mode? *Journal of Geophysical*
853 *Research*. [Online]. **121**(17),pp.10029–10042.

854 Stjern, C.W., Samset, B.H., Myhre, G., Forster, P.M., Hodnebrog, Ø., Andrews, T.,
855 Boucher, O., Faluvegi, G., Iversen, T., Kasoar, M., Kharin, V., Kirkevåg, A.,
856 Lamarque, J.F., Olivié, D., Richardson, T., Shawki, D., Shindell, D., Smith, C.J.,
857 Takemura, T. and Voulgarakis, A. 2017. Rapid Adjustments Cause Weak
858 Surface Temperature Response to Increased Black Carbon Concentrations.
859 *Journal of Geophysical Research: Atmospheres*. [Online]. **122**(21),pp.11,462-

11,481.

Tamarin-Brodsky, T. and Kaspi, Y. 2017. Enhanced poleward propagation of storms under climate change. *Nature Geoscience*. [Online]. **10**(12),pp.908–913.

Tang, T., Shindell, D., Faluvegi, G., Myhre, G., Olivié, D., Voulgarakis, A., Kasoar, M., Andrews, T., Boucher, O., Forster, P.M., Hodnebrog, Ø., Iversen, T., Kirkevåg, A., Lamarque, J. -F., Richardson, T., Samset, B.H., Stjern, C.W., Takemura, T. and Smith, C. 2019. Comparison of Effective Radiative Forcing Calculations Using Multiple Methods, Drivers, and Models. *Journal of Geophysical Research: Atmospheres*. [Online]. **124**(8),pp.4382–4394.

Thompson, D.W.J. and Solomon, S. 2002. Interpretation of recent Southern Hemisphere climate change. *Science*. **296**(5569),pp.895–899.

Voigt, A., Albern, N. and Papavasileiou, G. 2019. The atmospheric pathway of the cloud-radiative impact on the circulation response to global warming: Important and uncertain. *Journal of Climate*. [Online]. **32**(10),pp.3051–3067.

Voigt, A. and Shaw, T.A. 2015. Circulation response to warming shaped by radiative changes of clouds and water vapour. *Nature Geoscience*. [Online]. **8**(2),pp.102–106.

Voigt, A. and Shaw, T.A. 2016. Impact of regional atmospheric cloud radiative changes on shifts of the extratropical jet stream in response to global warming. *Journal of Climate*. [Online]. **29**(23),pp.8399–8421.

Yin, J.H. 2005. A consistent poleward shift of the storm tracks in simulations of 21st century climate. *Geophysical Research Letters*. [Online]. **32**(18),pp.1–4.

882 Zhao, X., Allen, R.J., Wood, T. and Maycock, A.C. 2020. Tropical Belt Width
883 Proportionately More Sensitive to Aerosols Than Greenhouse Gases.
884 *Geophysical Research Letters*. [Online]. **47**(7).

885

Tables

[K]	2xCO2	3xCH4	5xSO4	10xBC	2%Sol
Coupled	2.39 (1.58, 2.75)	0.70 (0.41, 1.13)	-1.82 (-0.93, -2.73)	0.85 (0.27, 1.68)	2.38 (1.53, 3.00)
fSST	0.28 (0.24, 0.35)	0.07 (0.03, 0.10)	-0.09 (-0.01, -0.16)	0.11 (0.02, 0.20)	0.15 (0.12, 0.18)

Table 1: Multi-model mean differences in global mean surface temperature [K] for the five perturbation experiments in the coupled and fSST configurations. Model spread is shown in brackets.

Figures

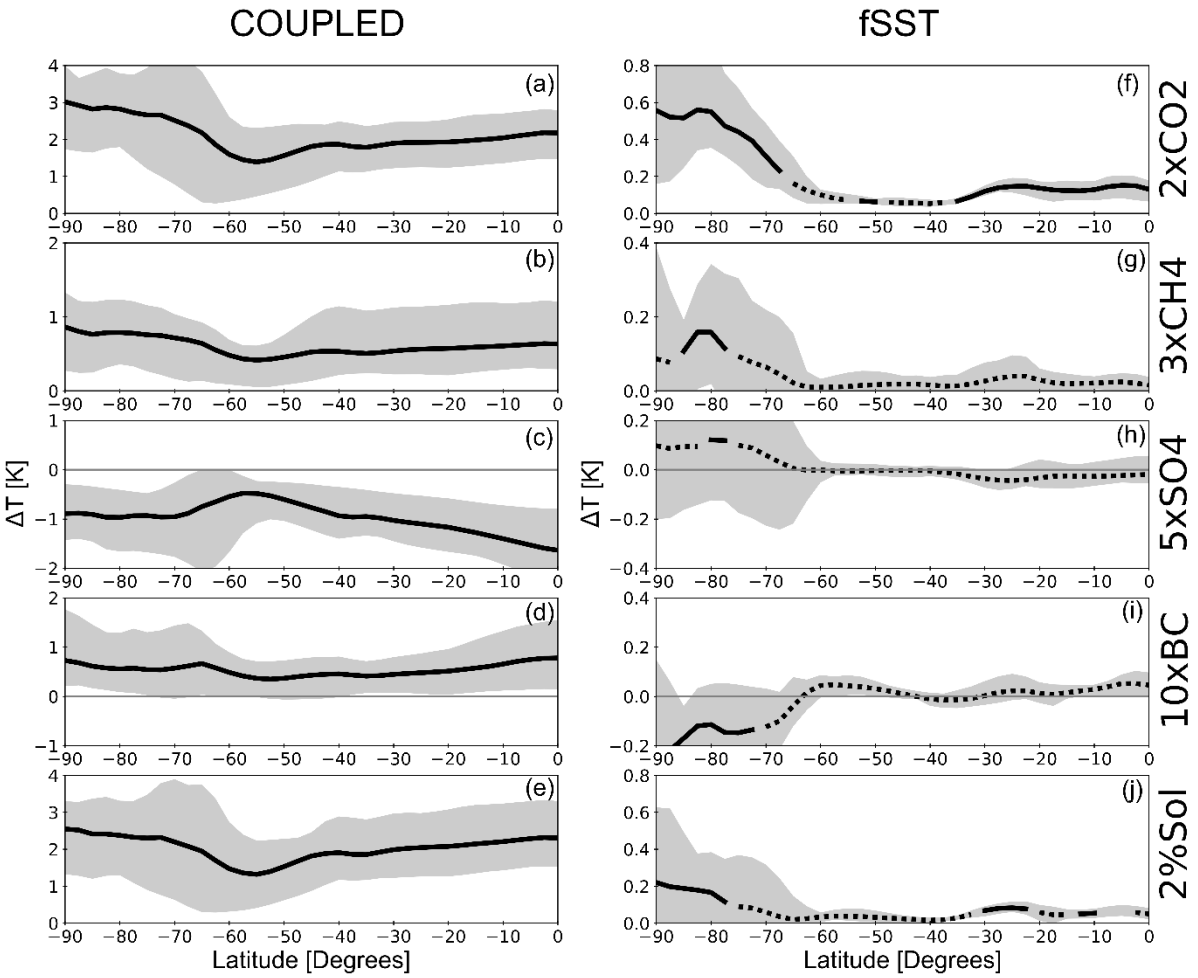

Figure 1: Southern hemisphere zonal mean near-surface temperature anomalies [K] in the five perturbation experiments (top-to-bottom: 2xCO2, 3xCH4, 5xSO4, 10xBC and 2%Sol) for (a-e) coupled experiments and (f-j) fixed SST experiments. Black line denotes the MMM and grey shading indicates model range. Solid lines indicate where the anomalies are significant at the 95% confidence level compared to internal variability (see Methods). Dashed lines show where the anomalies are not significant.

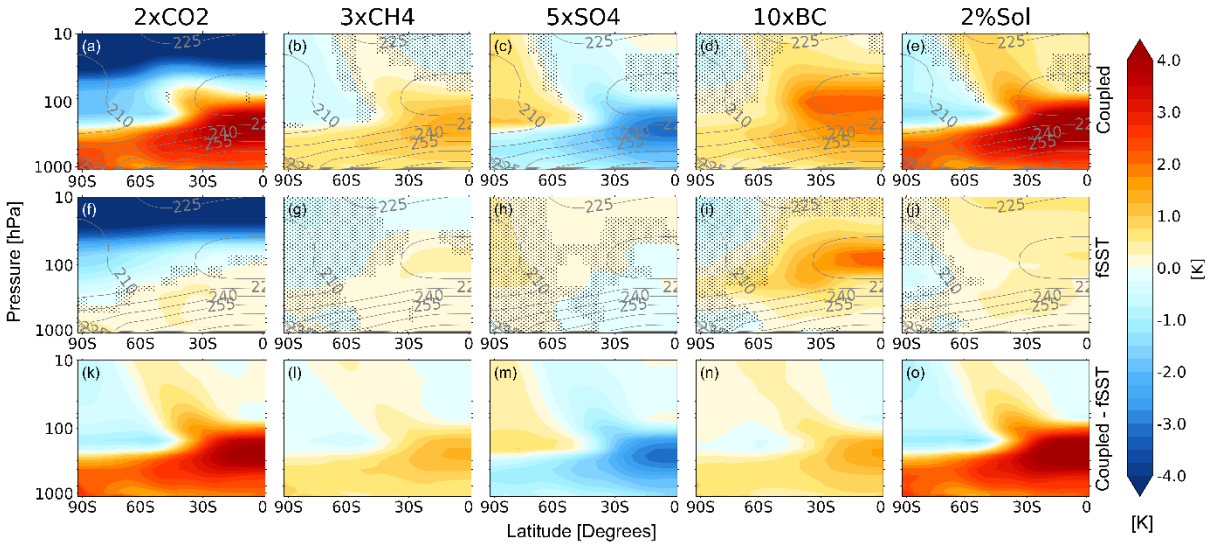

898

899 Figure 2: Annual and multi-model mean Southern hemisphere zonal mean
900 temperature anomalies [K] in the five perturbation experiments (left-to-right: 2xCO2,
901 3xCH4, 5xSO4, 10xBC and 2%Sol). (a-e) show the coupled experiments, (f-j) show
902 the fixed SST experiments, and (k-o) show the coupled minus fixed SST differences.
903 Stippling in top and middle rows denotes where one or more models disagrees on the
904 sign of the local anomaly. Grey contours show the control climatology.

905

906

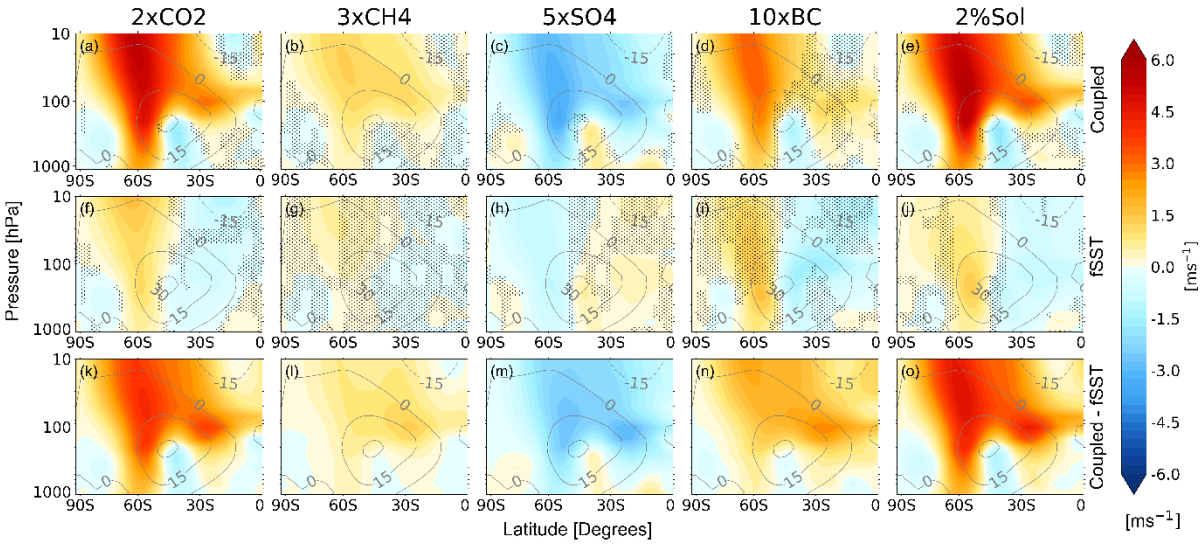

907

908 Figure 3: As in Figure 2, but for the $\overline{U}$ differences [m s^{-1}] in DJF.

909

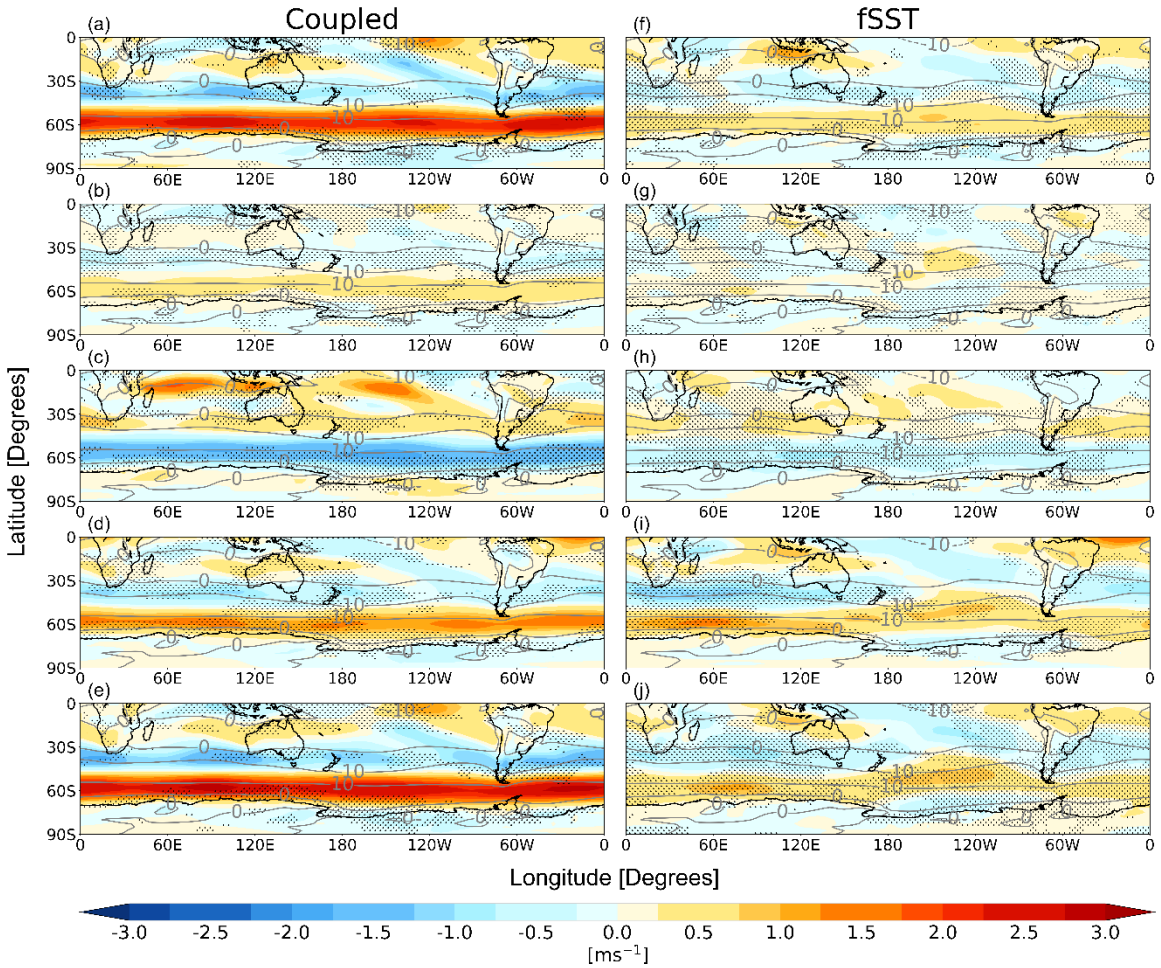

910

911 Figure 4: Multi-model mean Southern hemisphere DJF 850 hPa zonal wind anomalies
912 [m s^{-1}] in the five perturbation experiments (top-to-bottom: 2xCO2, 3xCH4, 5xSO4,
913 10xBC and 2%Sol) for (a-e) coupled experiments and (f-j) fixed SST experiments.
914 Stippling as in Figure 2. Grey contours show the control climatology.

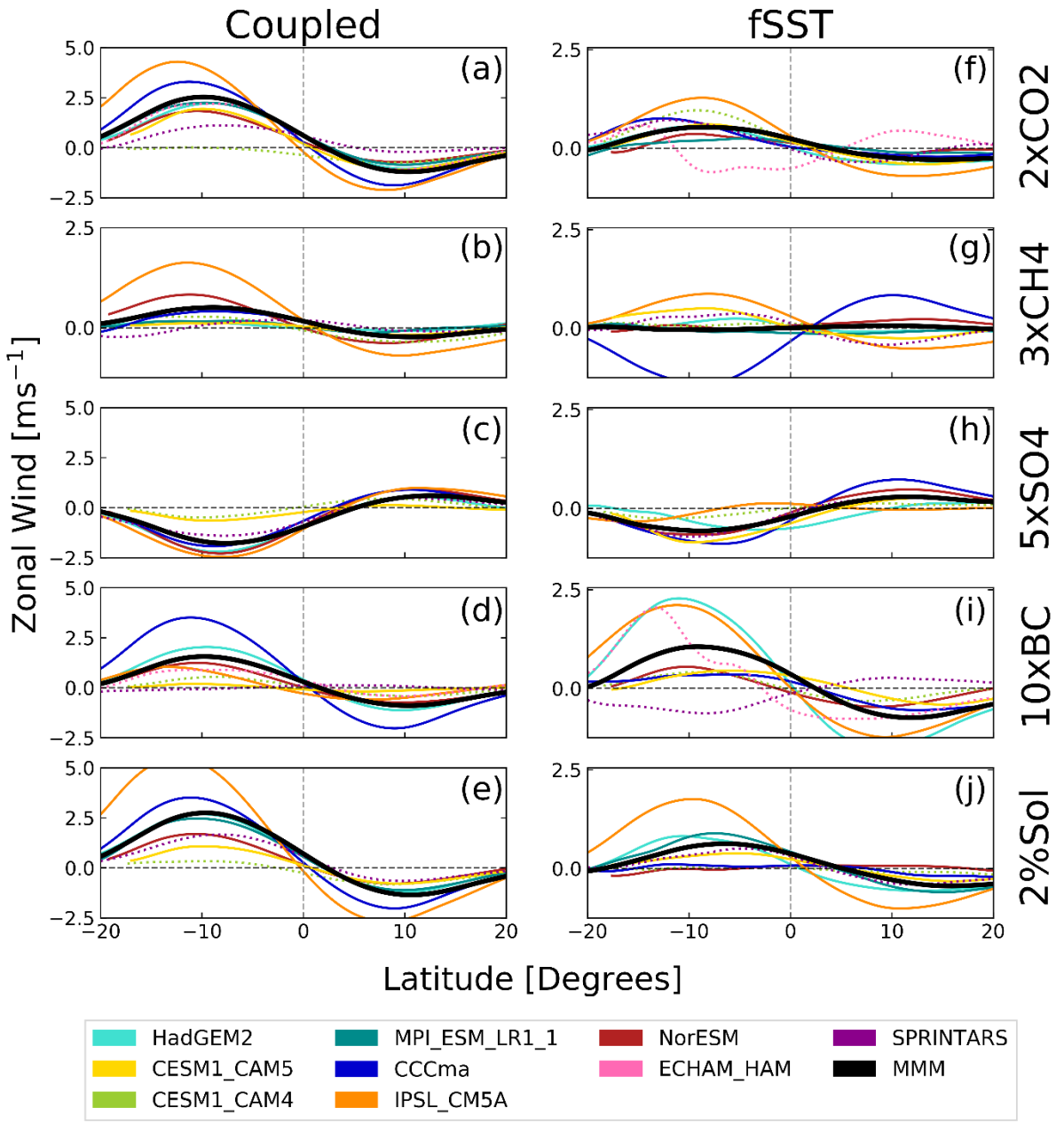

915

916 Figure 5: DJF 850 hPa $\overline{U}$ differences in the five perturbation experiments (top-to-
917 bottom: 2xCO2, 3xCH4, 5xSO4, 10xBC and 2%Sol) for individual models. (a-e) show
918 coupled experiments and (f-j) fixed SST experiments. The x-axis shows latitude
919 relative to the climatological EDJ maximum for each model. Dashed lines show models
920 that are excluded from the MMM calculation (see Methods).

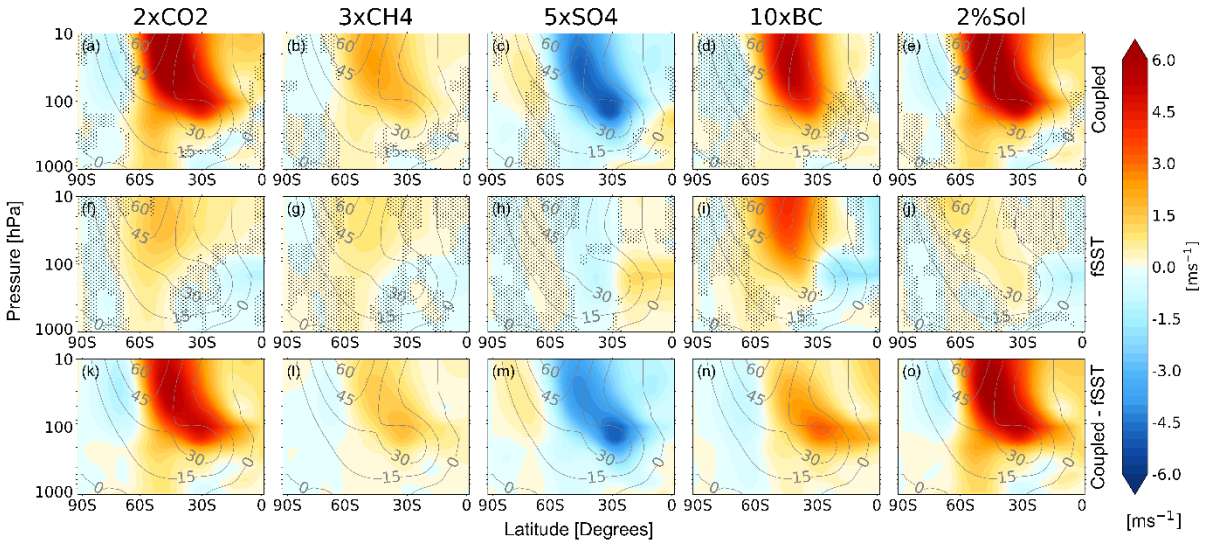

921

922 Figure 6: As in Figure 2, but for the $\bar{U}$ differences [m s^{-1}] in JJA.

923

924

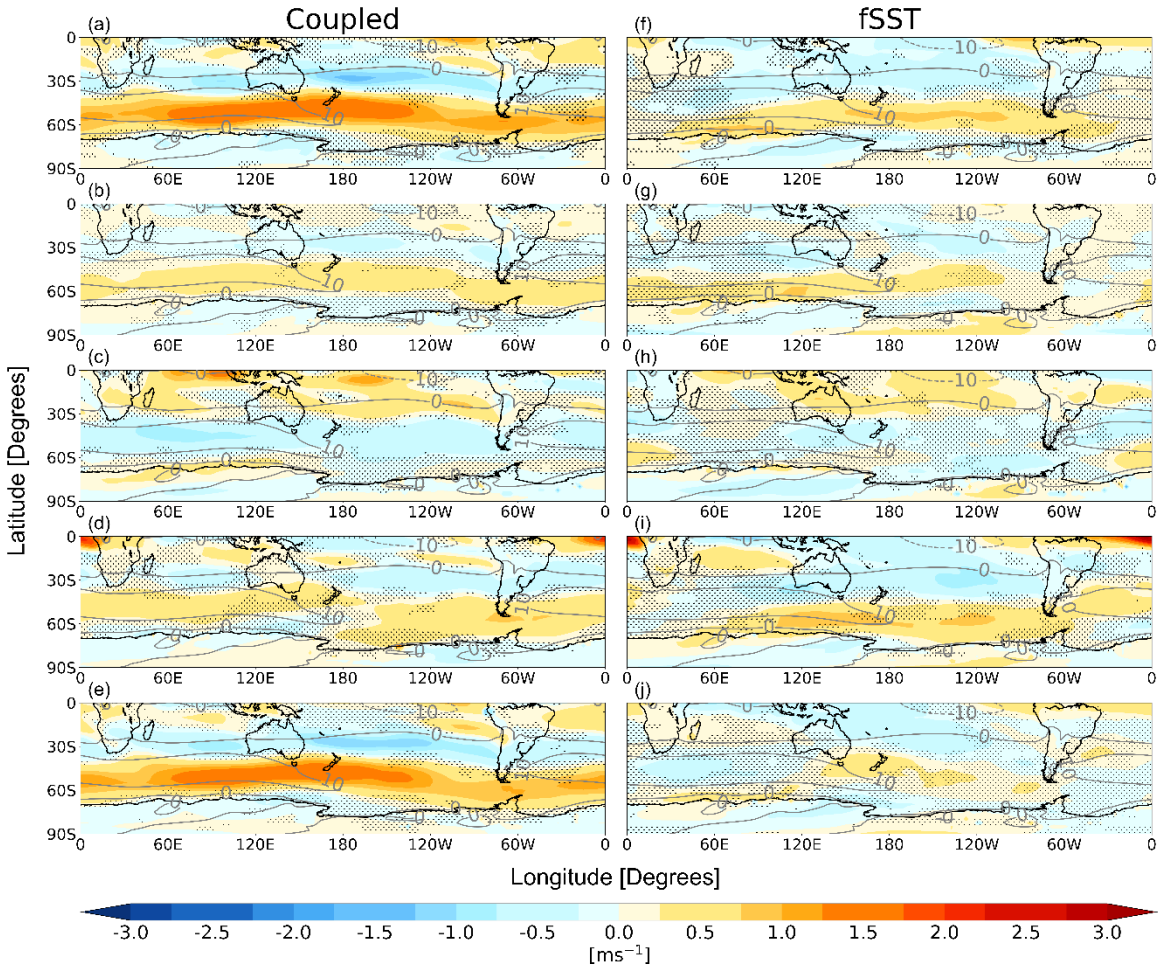

925

926 Figure 7: As in Figure 4, but for the U_{850} differences [m s^{-1}] in JJA.

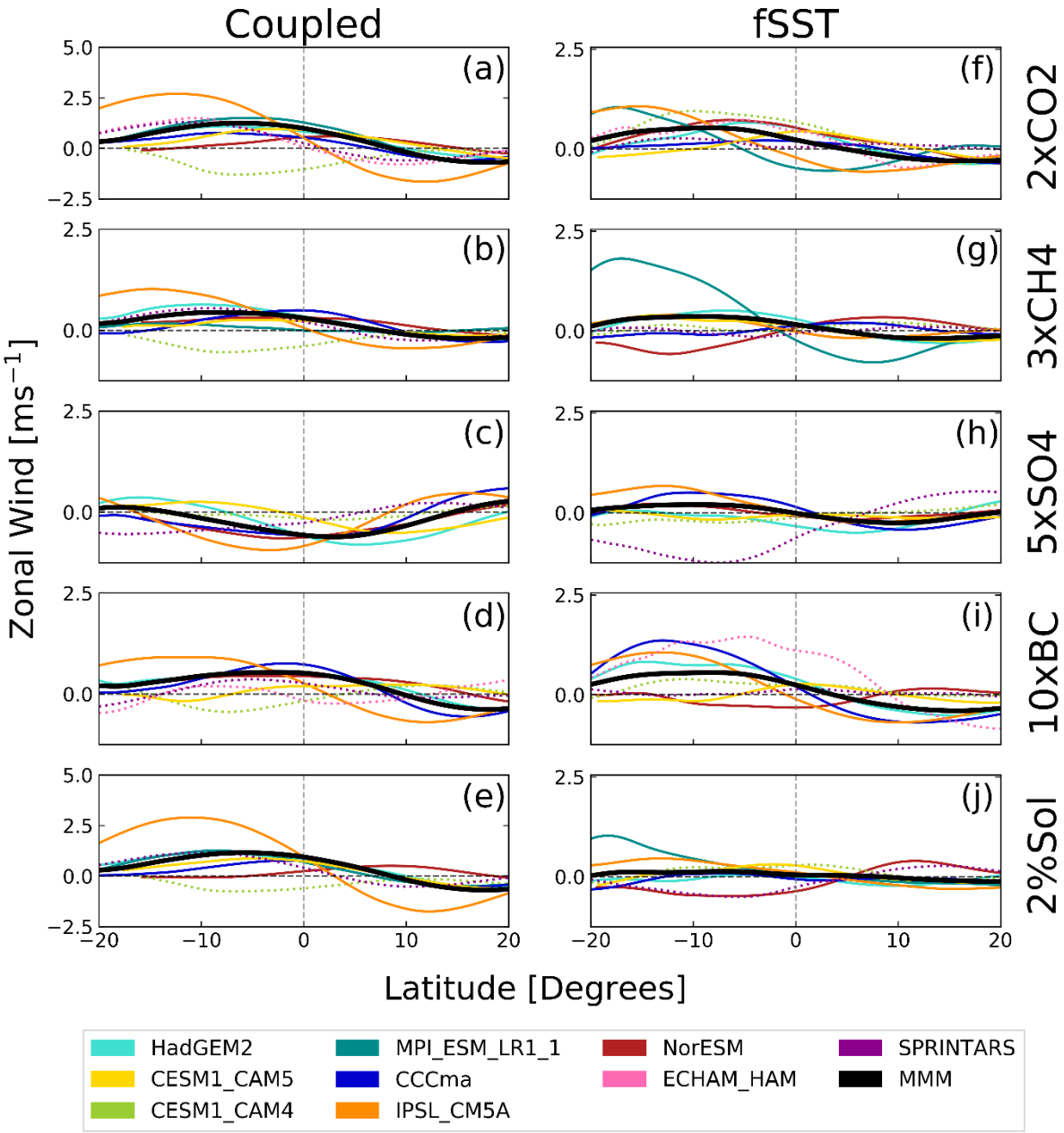

Figure 8: As in Figure 5, but for the 850 hPa $\bar{U}$ differences [m s^{-1}] in JJA.

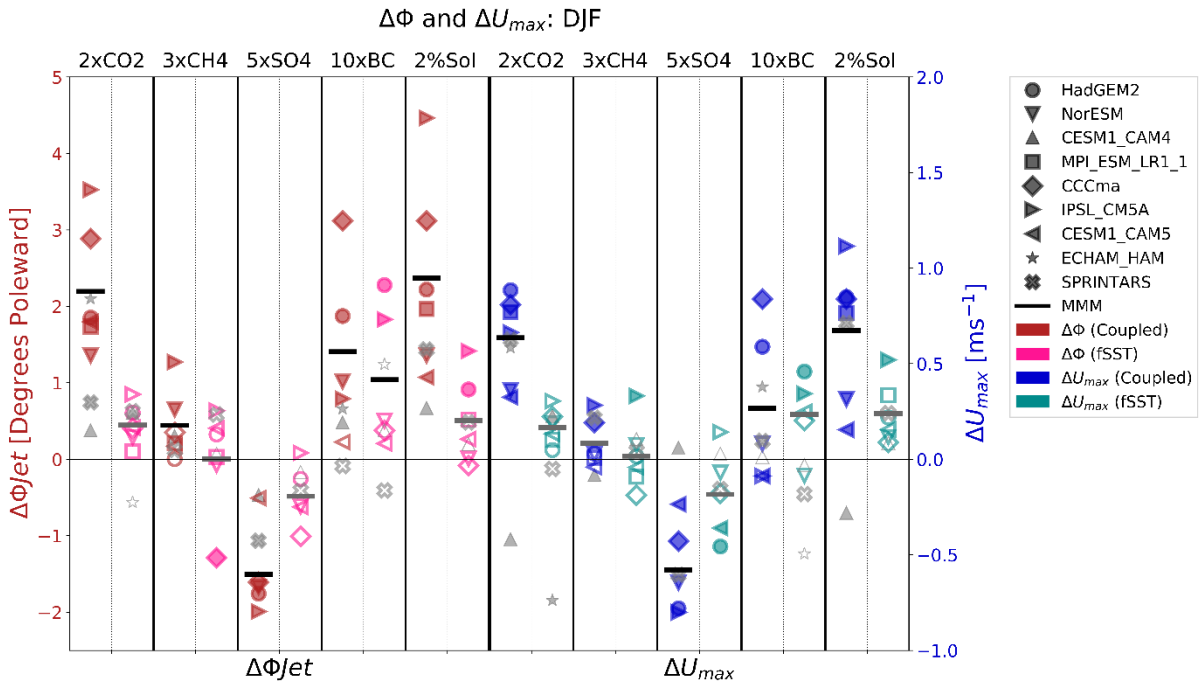

Figure 9: Southern hemisphere EDJ latitude and maximum speed anomalies in the five perturbation experiments in DJF. Coupled and fixed SST EDJ latitude shift anomalies are shown in red and pink (left y-axis), respectively, and coupled and fixed SST EDJ maximum speed anomalies are in blue and turquoise (right y-axis), respectively. Filled symbols denote changes that are significant at the 95% confidence level compared to internal variability (see Methods). The MMM is denoted by the solid line, which is black where the MMM change is significant at the 95% confidence level compared to the median internal variability or grey otherwise. Slab ocean models and SPRINTARS that are not included in the MMM calculation are shown in grey.

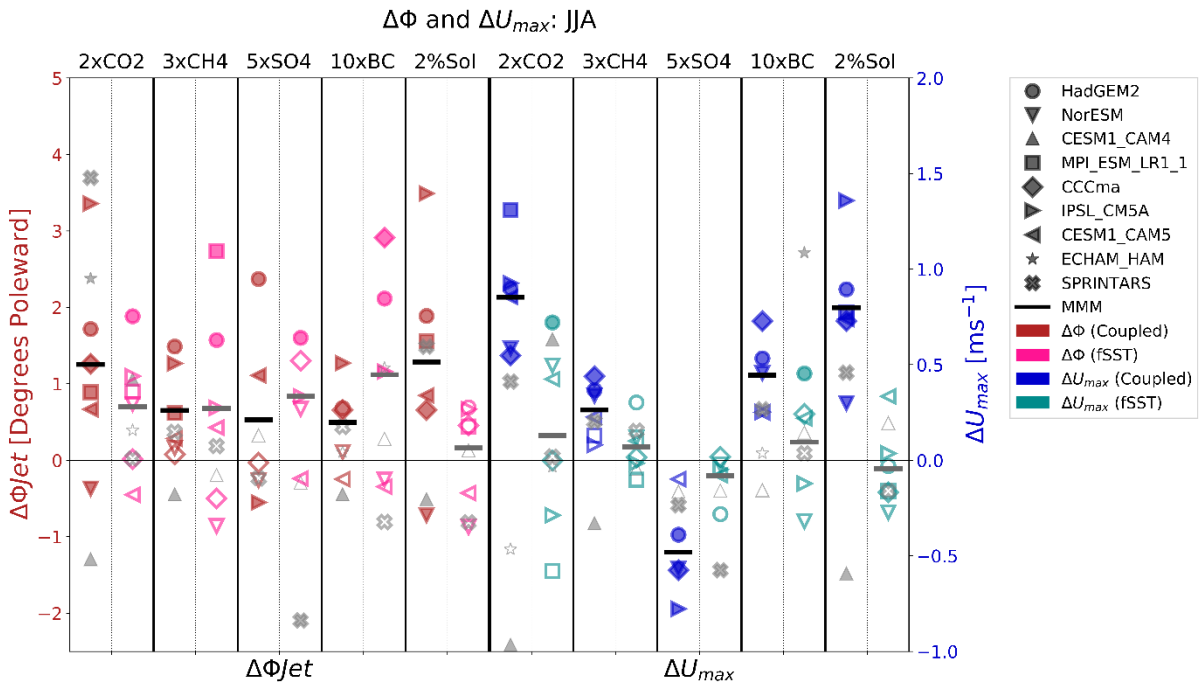

941

942 Figure 10: As in Figure 9 but for JJA.

943

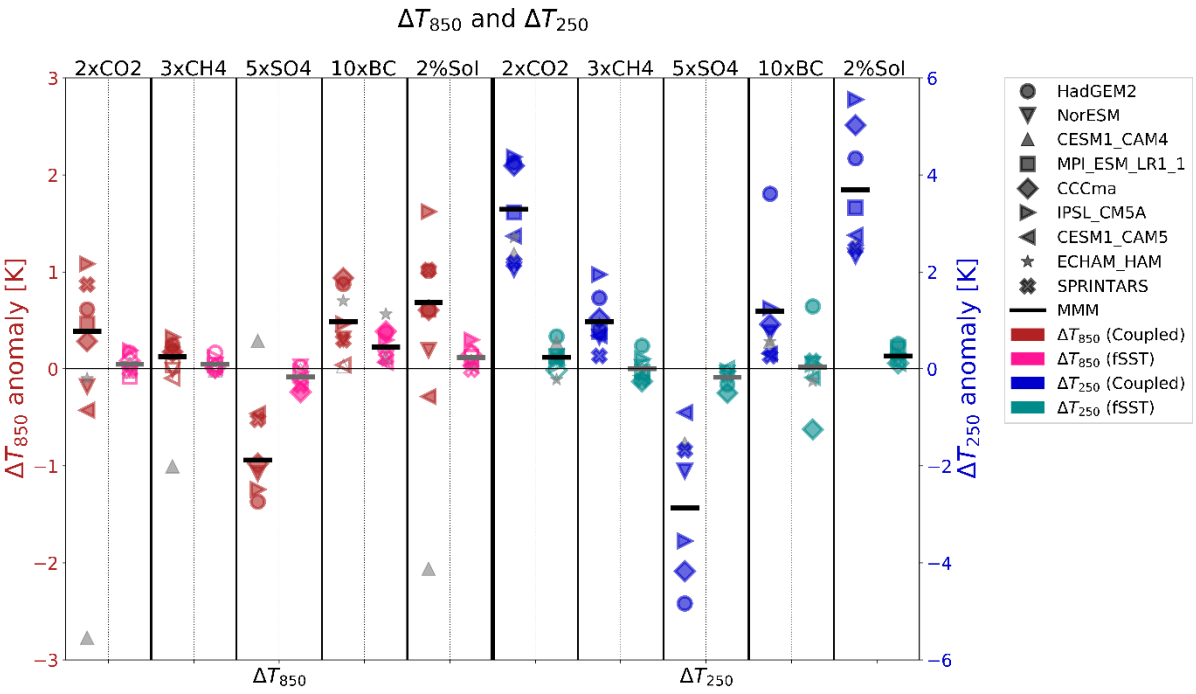

Figure 11: Annual mean 850 hPa and 250 hPa meridional temperature gradient changes (30°N-30°S minus 60°S - 90°S) in the five perturbation experiments. ΔT_{850} coupled and fixed SST anomalies are shown in red and pink (left y-axis), respectively, and ΔT_{250} coupled and fixed SST anomalies are in blue and turquoise (right y-axis), respectively. Filled symbols denote changes that are significant at the 95% confidence level compared to internal variability (see Methods). The MMM is denoted by the solid line, which is black where the MMM change is significant at the 95% confidence level compared to the median internal variability or grey otherwise. Slab ocean models that are not included in the MMM calculation are shown in grey.

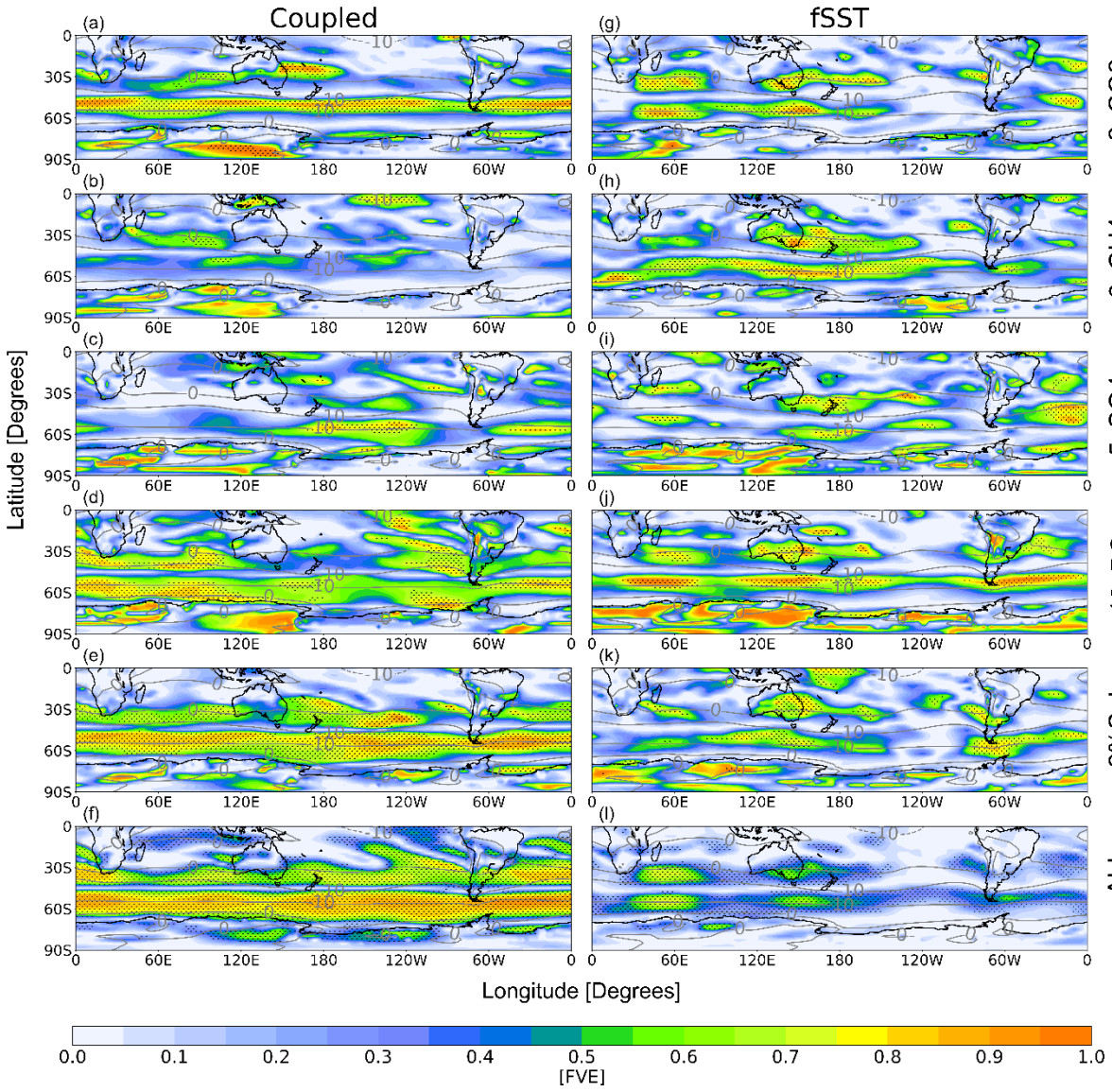

Figure 12: The fraction of inter-model variance in ΔU_{850} explained by the regression onto ΔT_{850}, defined as the coefficient of determination (R^2). Stippling indicates where the correlation is statistically significant ($P < 0.05$).

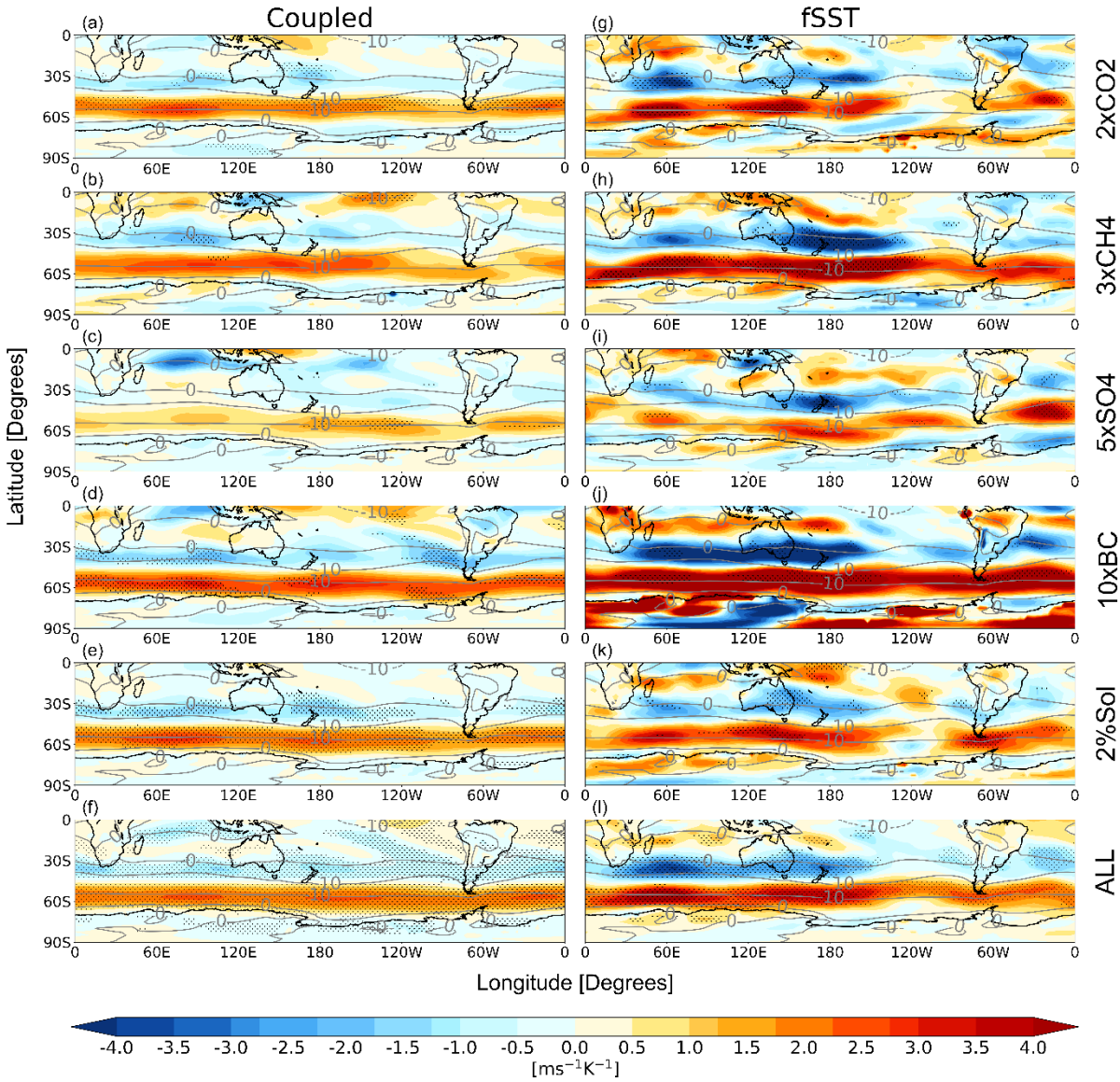

961

962 Figure 13: Inter-model regression of DJF ΔU_{850} vs. DJF ΔT_{850} [m s^{-1} K^{-1}] for the five
963 perturbation experiments and (bottom) across all experiments. (a-f) show the
964 coupled experiments and (g-l) show the fixed SST experiments. Stippling as in
965 Figure 12.